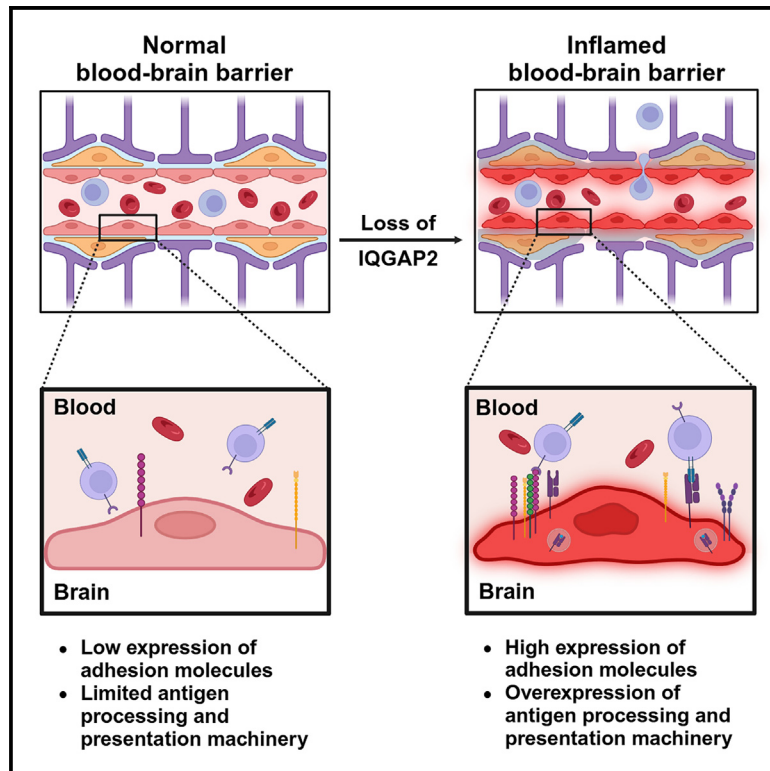**Article**

IQGAP2 regulates blood-brain barrier immune dynamics

Graphical abstract

Authors

Ketaki A. Katdare, Andrew Kjar, Natasha M. O'Brown, ..., Matthew S. Schrag, Sean G. Megason, Ethan S. Lippmann

Correspondence

ethan.s.lippmann@vanderbilt.edu

In brief

Neuroscience; Immunology

Highlights

- IQGAP2 regulates immune cell infiltration into the central nervous system

- Global loss of IQGAP2 alters inflammatory transcriptome in brain endothelial cells

- Alzheimer's disease is associated with reduced hippocampal IQGAP2 levels

CellPress

iScience

Article

IQGAP2 regulates blood-brain barrier immune dynamics

Ketaki A. Katdare,[1] Andrew Kjar,[2] Natasha M. O'Brown,[3] Emma H. Neal,[4] Alexander G. Sorets,[2] Alena Shostak,[5] Wilber Romero-Fernandez,[5] Alexander J. Kwiatkowski,[4] Kate Mlouk,[4] Hyosung Kim,[4] Rebecca P. Cowell,[4] Katrina R. Schwensen,[4] Cristian O. Carvajal Tapia,[5] Guste Venslovaite,[4] Kensley B. Horner,[4] John T. Wilson,[2,4] Matthew S. Schrag,[1,5,6] Sean G. Megason,[3] and Ethan S. Lippmann[1,2,4,5,6,7,*]

[1]Vanderbilt Brain Institute, Vanderbilt University, Nashville, TN, USA
[2]Department of Biomedical Engineering, Vanderbilt University, Nashville, TN, USA
[3]Department of Systems Biology, Harvard Medical School, Boston, MA, USA
[4]Department of Chemical and Biomolecular Engineering, Vanderbilt University, Nashville, TN, USA
[5]Department of Neurology, Vanderbilt University Medical Center, Nashville, TN, USA
[6]Vanderbilt Memory and Alzheimer's Center, Vanderbilt University Medical Center, Nashville, TN, USA
[7]Lead contact
*Correspondence: ethan.s.lippmann@vanderbilt.edu
https://doi.org/10.1016/j.isci.2025.111994

SUMMARY

Brain endothelial cells (BECs) play an important role in maintaining central nervous system (CNS) homeostasis through blood-brain barrier (BBB) functions. BECs express low baseline levels of adhesion receptors, which limits entry of leukocytes. However, the molecular mediators governing this phenotype remain mostly unclear. Here, we explored how infiltration of immune cells across the BBB is influenced by the scaffold protein IQ motif containing GTPase-activating protein 2 (IQGAP2). In mice and zebrafish, we demonstrate that loss of Iqgap2 increases infiltration of peripheral leukocytes into the CNS under homeostatic and inflammatory conditions. Using single-cell RNA sequencing and immunohistology, we further show that BECs from mice lacking Iqgap2 exhibit a profound inflammatory signature, including extensive upregulation of adhesion receptors and antigen-processing machinery. Human tissue analyses also reveal that Alzheimer's disease is associated with reduced hippocampal IQGAP2. Overall, our results implicate IQGAP2 as an essential regulator of BBB immune privilege and immune cell entry into the CNS.

INTRODUCTION

Maintenance of central nervous system (CNS) homeostasis is crucial for ensuring normal functions in neurons and glial cells, which are sensitive to exogenous molecules in circulation.[1] The brain is insulated from these factors with the help of a specialized partition known as the blood-brain barrier (BBB). The BBB is composed of barrier-forming brain endothelial cells (BECs) with unique cellular machinery that regulate the entry of macromolecules and solutes into the brain,[2] including transporters that control the bidirectional exchange of nutrients and waste and tight junctions that prevent passive leakage of blood components into the brain.[3]

In addition to modulating molecular transport, BECs also act as a selective interface between the peripheral immune system and the brain.[4] Until recently, the CNS was considered to be completely isolated from the peripheral immune system and therefore an immune-privileged organ.[5,6] However, recent evidence shows that the CNS is under constant immune surveillance to identify and resolve mediators of injury.[7,8] For example, microglia are tissue-resident innate immune cells that continually inspect the CNS parenchyma.[9,10] Further, interstitial fluid and cerebrospinal fluid provide drainage pathways for prospective antigens to reach

the periphery and stimulate immune cells.[11–14] As such, initiation of an inflammatory response in the CNS can lead to recruitment of leukocytes across the BBB. BECs facilitate this process through the expression of various receptors, such as leukocyte adhesion molecules (LAMs), that allow interactions with and extravasation of leukocytes into tissue beds.[15,16] In addition, BEC chemokine signaling and antigen presentation[17–19] also play a key role in orchestrating leukocyte extravasation. Although the underlying molecular mechanisms of leukocyte extravasation are similar across all organs, BECs have been shown to express very low levels of LAMs under homeostatic conditions, making them refractory to mild inflammatory cues.[1,20] However, despite several exquisite single-cell RNA sequencing (scRNA-seq) studies identifying differentially expressed genes between BECs and peripheral endothelial cells,[21–26] as well as scRNA-seq profiles of different cell types in the neurovascular unit,[24,25] the mechanisms underlying suppression of LAM expression in BECs and general limitation of immune cell extravasation across the BBB remain poorly understood.

IQ motif containing GTPase-activating protein 1 (IQGAP1), a ubiquitously expressed scaffolding protein, has been recently implicated in facilitating leukocyte trafficking across peripheral endothelium.[27,28] Historically, IQGAP1 was known as a regulator
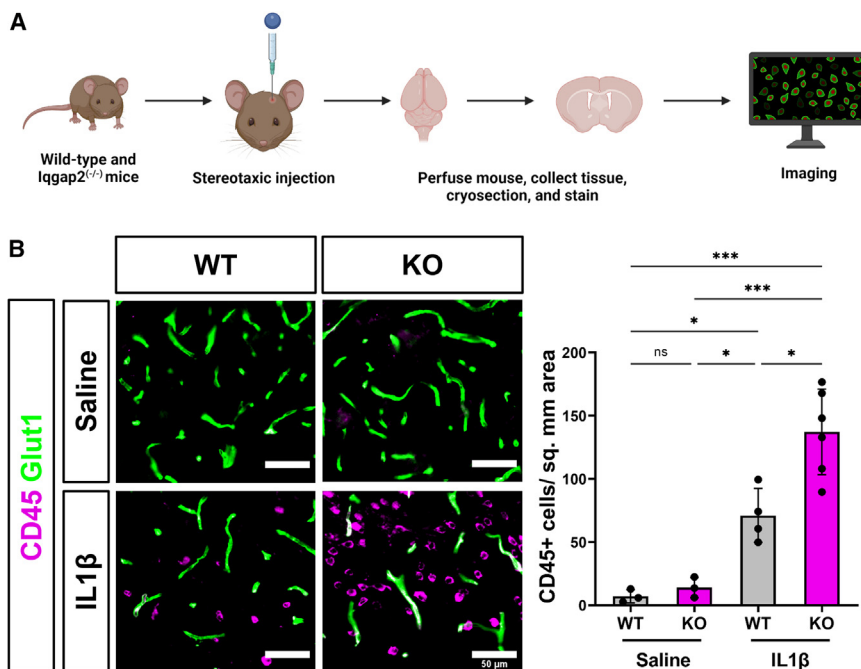
A

B

Figure 1. Global loss of Iqgap2 increases infiltration of peripheral leukocytes in a mouse model of acute neuroinflammation

(A) Schematic representation of experimental design for assessing leukocyte numbers in mouse brains 24 h after intracerebroventricular saline or IL-1β delivery.

(B) Representative images and quantification of CD45$^+$ immune cells (magenta) and vasculature (green) in wild-type (WT) and Iqgap2$^{-/-}$ (KO) mouse brain cortex following treatment with saline or IL-1β. Scale bars represent 50 μm. Data are represented as mean ± SD, and each data point represents an individual mouse, where at least five images were quantified per mouse. For saline treatment, $N = 3$ WT mice and $N = 3$ KO mice, and for IL-1β treatment, $N = 4$ WT mice and $N = 6$ KO mice. Statistical significance was calculated using two-way ANOVA with Tukey's multiple comparison's test (*$p < 0.05$; ***$p < 0.001$).

of cellular signaling due to its role as a scaffolding protein.[29] It also acts as an oncogene driving hepatocellular carcinogenesis.[30,31] Interestingly, IQ motif containing GTPase-activating protein 2 (IQGAP2), a related member of the same scaffolding protein family, acts as a tumor suppressor to counteract the oncogenic effects of IQGAP1,[32,33] and Iqgap2$^{-/-}$ mice develop spontaneous hepatocellular carcinomas (but otherwise exhibit no histological defects at younger ages).[33] Since IQGAP2 is believed to suppress IQGAP1 function, and IQGAP2 expression is predicted in multiple neurovascular support cells such as astrocytes and microglia based on transcriptional profiling studies,[21,34–36] we hypothesized that IQGAP2 may influence inflammatory responses and leukocyte extravasation at the BBB. Herein, using multiple *in vivo* models, we show that loss of Iqgap2 increases leukocyte infiltration into the CNS under various conditions. scRNA-seq of BECs from wild-type (WT) and Iqgap2$^{-/-}$ mice reveals an upregulation of multiple inflammatory genes and signaling pathways involved in BBB-immune cell interactions. Further, using postmortem human brain tissue, we determined that IQGAP2 was reduced in the hippocampus of patients with Alzheimer's disease (AD). Overall, our results benchmark IQGAP2 as a key molecular player involved in BBB-immune crosstalk and leukocyte entry into the CNS.

RESULTS

Global loss of Iqgap2 increases peripheral immune cell infiltration into the brain in a mouse model of acute neuroinflammation

To initially assess whether murine Iqgap2 influences leukocyte infiltration into the brain, we delivered interleukin-1 beta (IL-1β) into the lateral ventricles of WT and Iqgap2$^{-/-}$ mice (129S background) to induce acute neuroinflammation.[37,38] After 24 h, infiltration of leukocytes was assessed by immunohistochemical

labeling of CD45$^+$ cells in cortical brain sections. We measured a significant increase in the number of CD45$^+$ cells in the cortex of Iqgap2$^{-/-}$ mice as compared to their WT littermates (Figure 1A). We also confirmed that delivery of saline to the lateral ventricles in a similar fashion did not stimulate CD45$^+$ cell infiltration into the brains of both WT and Iqgap2$^{-/-}$ mice (Figure 1B). These data suggest that Iqgap2 constrains leukocyte infiltration into the mouse CNS following a central inflammatory challenge.

Global loss of Iqgap2 increases immune cell infiltration in experimental autoimmune encephalomyelitis

As dysregulated immune cell infiltration is a hallmark of several neurodegenerative conditions,[39–45] we sought to next evaluate whether loss of Iqgap2 affects immune cell access to the CNS in the presence of an inflammatory neurodegenerative condition. As such, to monitor the effects of Iqgap2 loss under a chronic inflammatory insult,[46] we induced experimental autoimmune encephalomyelitis (EAE) in WT and Iqgap2$^{-/-}$ 129S mice (Figure 2A). To validate our experimental strategy, we concurrently induced EAE in C57BL/6 mice and observed robust development of disease (Figure S1). We measured a significant increase in CD45$^+$ cells in the Iqgap2$^{-/-}$ lumbar spinal cord compared to WT 129S mice 30 days after EAE induction (Figure 2B). Interestingly, this increase in infiltrating leukocytes did not produce significant differences in disease severity, probability of survival, or demyelination (Figures 2C–2E), suggesting the infiltration events may be decoupled from pathology. Overall, these data further indicate that loss of Iqgap2 contributes to increased leukocyte extravasation into the CNS under extended neuroinflammation.

Loss of Iqgap2 increases infiltration of peripheral immune cells into the brain in zebrafish in the absence of inflammation

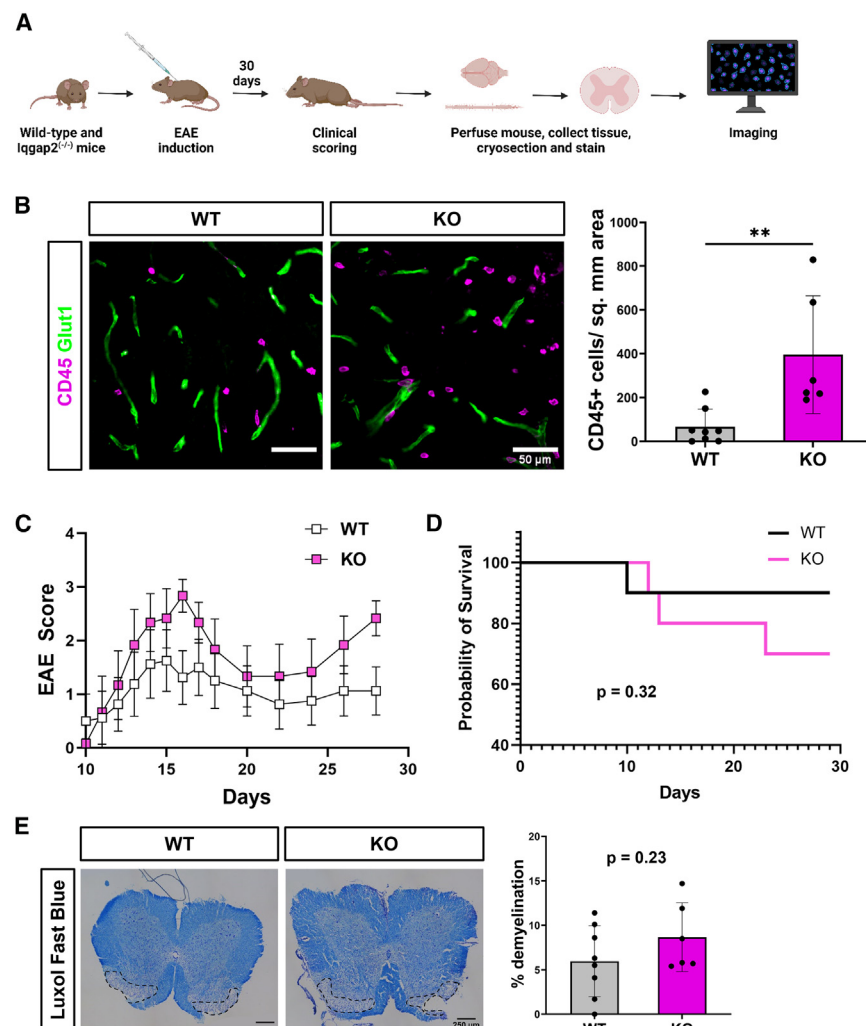Our data in multiple inflammatory mouse models suggest that Iqgap2 plays an important role in BBB immune privilege. To

A

Wild-type and Iqgap2(-/-) mice → EAE induction → 30 days → Clinical scoring → Perfuse mouse, collect tissue, cryosection and stain → Imaging

B

Figure 2. Global loss of Iqgap2 increases infiltration of peripheral leukocytes in EAE

(A) Schematic representation of experimental design for assessing response to EAE 30 days following induction.

(B) Representative images and quantification of CD45$^+$ immune cells (magenta) and vasculature (green) in wild-type (WT) and Iqgap2$^{-/-}$ (KO) lumbar spinal cord at 30 days following EAE induction. Scale bars represent 50 μm. Data are represented as mean ± SD, and each data point represents an individual mouse. At least eight images were quantified per mouse. N = 8 WT mice, N = 6 KO mice. Statistical significance was calculated using the unpaired Student's t test (**p < 0.01).

(C) EAE score curve for wild-type (WT) and Iqgap2$^{-/-}$ (KO) mice following EAE induction. Data are presented as mean ± SEM. N = 8 WT mice, N = 6 KO mice. Statistical significance was calculated using the unpaired Student's t test on area under the curve.

(D) Probability of survival in WT versus KO mice following EAE induction. N = 10 WT and KO mice. Statistical significance was calculated using Log rank (Mantel-Cox) test.

(E) Representative images and quantification of demyelinating lesions in WT and KO lumbar spinal cord section stained with Luxol fast blue at 30 days following EAE induction. Scale bars represent 250 μm. Data are represented as mean ± SD, and each data point represents an individual mouse, where one image was quantified per mouse. N = 8 WT mice, N = 6 KO mice. Statistical significance was calculated using the unpaired Student's t test.

C

D

E

corroborate these findings in an additional species, we generated zebrafish crispants by direct injection of Cas9 protein with multiple single-guide RNAs (sgRNAs) to target genes of interest in single-cell embryos with both endothelial cells (kdrl:mCherry) and immune cells (mpeg1:EGFP) transgenically labeled. We specifically assessed the presence of mpeg+ macrophage lineage cells in the brains of 5 days post-fertilization (dpf) zebrafish, which have a functional BBB,[47] that were either uninjected or targeting *tyr* or *iqgap2.* Although uninjected fish are expected to retain normal function of all genes, *tyr* crispants should have mosaic knockout of tyrosinase*,* a protein involved in pigment production that is not expected to affect leukocyte infiltration; this serves as an additional CRISPR injection control. Both controls displayed similarly low numbers of mpeg+ cells in the brain, whereas *iqgap2* crispants displayed a significant increase in the number of mpeg+ cells (Figure 3B). Since mpeg also labels brain resident microglia, we used an established method to label microglia with Neutral Red dye[48] and distinguish these cells from infiltrating leukocytes. Uninjected controls and *iqgap2* crispants were therefore treated with Neutral Red, and all mpeg+/Neutral Red+ double-positive microglia and mpeg+/Neutral Red−

infiltrating leukocytes were quantified throughout the entire zebrafish brain. We measured a significant increase in the total number of mpeg+ cells, similar to previous experiments, but not double-positive microglia in the *iqgap2* crispants, and the number of mpeg+/Neutral Red− infiltrating leukocytes was significantly increased (Figure 3C). These data suggest that *iqgap2* is essential for restricting the infiltration of leukocytes into the CNS under homeostatic conditions in zebrafish, as its mosaic depletion enhanced the entry of peripheral leukocytes into the brain.

Global loss of Iqgap2 yields a profound inflammatory transcriptomic profile in mouse BECs

Our data indicate that Iqgap2 plays an important role in restricting peripheral immune access to the CNS and in modulating responses to inflammatory insults. Iqgap2 is a large scaffolding protein known to orchestrate many different cellular functions such as regulating cytoskeletal organization, cytokinesis, and carcinogenesis,[29] suggesting it could govern many different signaling axes that would influence BBB function and cellular crosstalk within the neurovascular unit. After confirming general expression of Iqgap2 in mouse brain and enriched vessel fractions (Figure S2), we performed scRNA-seq on BECs isolated
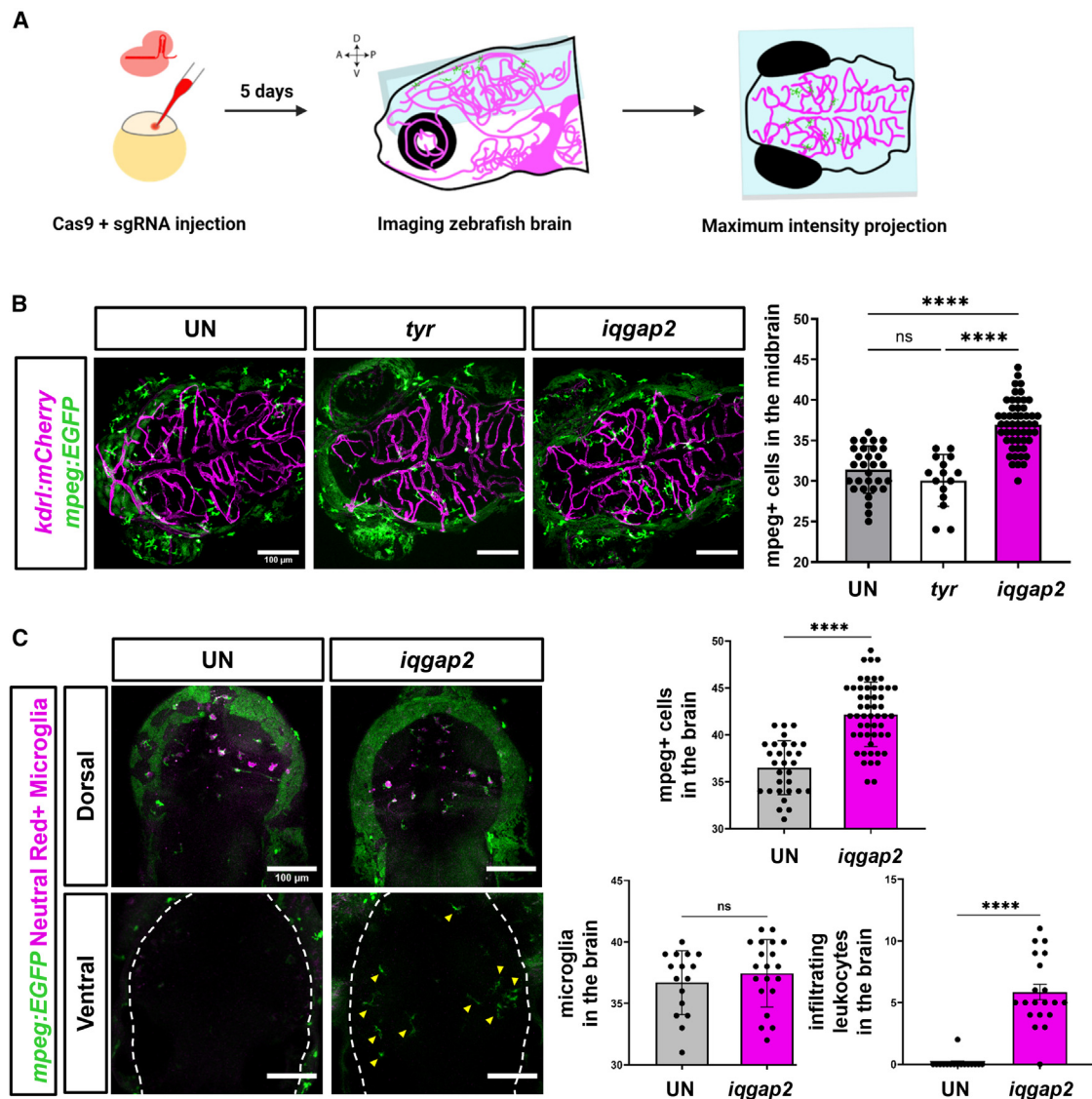
Figure 3. Mosaic loss of *iqgap2* expression increases infiltration of peripheral immune cells into the zebrafish brain

(A) Schematic representation of experimental design for assessing leukocyte numbers in the larval zebrafish brain. Double transgenic (kdrl:mCherry; mpeg:EGFP) single-cell embryos were injected with Cas9 protein and sgRNAs to target genes of interest. These mosaic crispants were then allowed to develop normally, and mpeg+ leukocytes were quantified in the brain at 5 dpf.

(B) Representative 100-μm thick maximum intensity projection images and quantification of macrophage lineage cells (mpeg:EGFP) in the brains of uninjected (UN) controls, *tyr* crispant controls, and *iqgap2* crispants. Vasculature is marked with the kdrl:mCherry transgene (magenta). Scale bars represent 100 μm. Data are represented as mean ± SD, and each data point represents an individual fish. *N* = 30 fish (UN), 15 fish (*tyr*), and 52 fish (*iqgap2*). Statistical significance was calculated using a one-way ANOVA with Tukey's multiple comparison's test (****p < 0.0001).

(C) Representative images and quantification of infiltrating leukocytes versus tissue-resident microglia in the brains of *iqgap2* crispants versus uninjected (UN) controls. Representative 30-μm thick maximum intensity projection images of the dorsal (top) or ventral (bottom) brain regions and quantification of mpeg+ (green) macrophage lineage cells and mpeg+/Neutral Red+ (magenta) microglia. Yellow arrowheads indicate individual mpeg+/Neutral Red− infiltrating leukocytes in the ventral brain of *iqgap2* crispants. Scale bars represent 100 μm. Data represented as mean ± SD, and each data point represents an individual fish. *N* = 16 fish (UN) and 20 fish (*iqgap2*). Statistical significance was calculated using an unpaired Student's t test (****p < 0.0001).

from WT and Iqgap2$^{−/−}$ mice to better understand how loss of Iqgap2 affects BBB function. Here, to generate an endothelial-cell-enriched population for sequencing, we isolated antibody-labeled CD31$^+$ cells from dissociated mouse brains using fluorescence-activated cell sorting (Figure 4A). After implement-

ing quality control metrics, cells were first analyzed using dimension-reduction by uniform manifold approximation and projection (UMAP) and unsupervised clustering to obtain 12 unique identities: endothelial cells (ECs), PLVAP-expressing endothelial cells (EC_plvap), hemoglobin-expressing endothelial
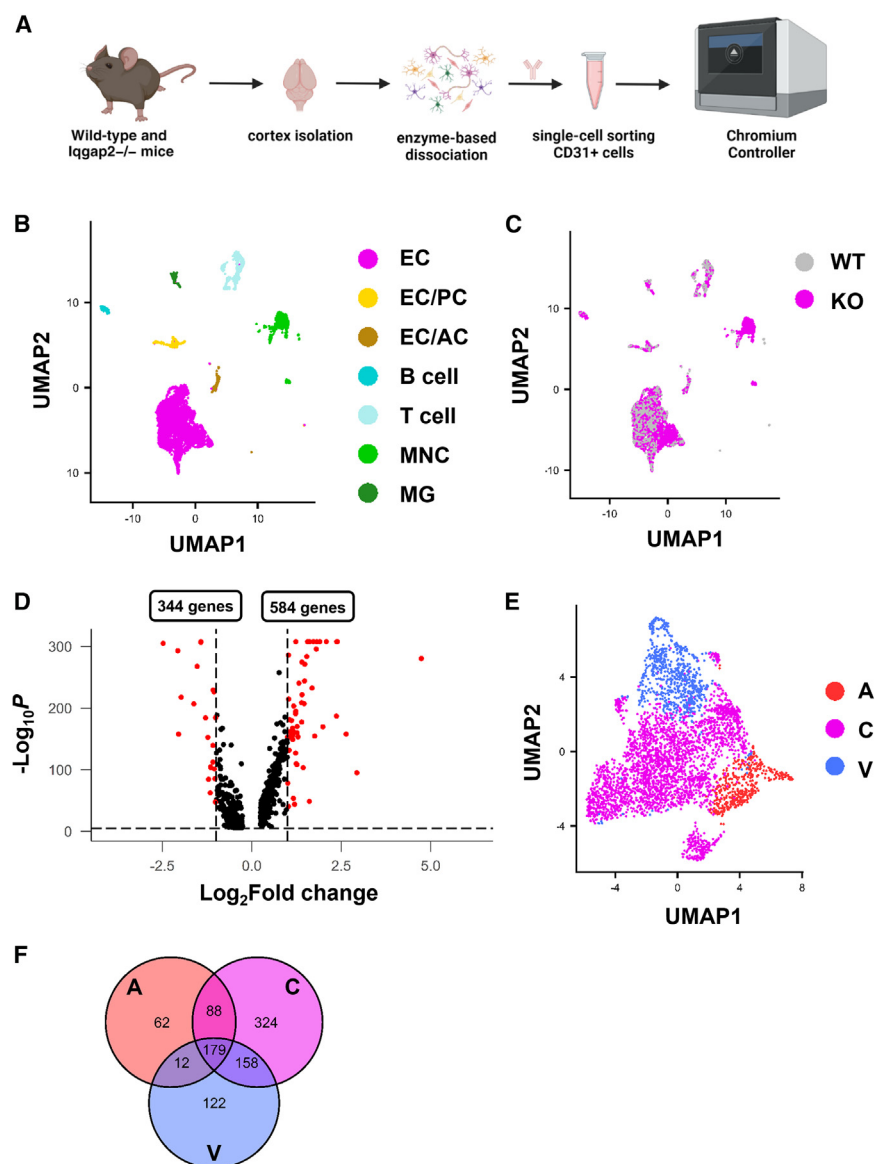
A

Wild-type and Iqgap2–/– mice → cortex isolation → enzyme-based dissociation → single-cell sorting CD31+ cells → Chromium Controller

B

EC
EC/PC
EC/AC
B cell
T cell
MNC
MG

C

WT
KO

D

344 genes   584 genes

E

A
C
V

F

Figure 4. Global loss of Iqgap2 yields extensive transcriptional changes in BECs

(A) Schematic representation of experimental design. Whole-brain cortices were isolated from wild-type (WT) and Iqgap2$^{-/-}$ (KO) mice, dissociated to a single-cell suspension using enzyme-based dissociation techniques, and sorted to enrich for CD31$^+$ cells before sequencing.

(B) UMAP cell annotations based on unsupervised clustering. EC, endothelial cells; EC/PC, EC/stromal cells (pericytes); EC/AC, EC/stromal cells (astrocytes); MNC, monocytes; MG, microglia.

(C) UMAP comparison between WT (gray) and KO (pink) cells.

(D) Volcano plot highlighting differentially expressed genes in the EC cluster; 928 genes were significantly altered, with 584 upregulated and 344 downregulated by loss of Iqgap2. Red dots indicate genes with $p < 0.05$ and >2-fold change in expression.

(E) UMAP of endothelial zonal identity based on unsupervised clustering. A, arterial; C, capillary; V, venous.

(F) Venn diagram showing number of DEGs shared between zonal identities.

ined these DEGs along the neurovascular tree. We used unsupervised clustering to subcluster BECs into six sub-populations, and based on marker gene expression, these subclusters were further classified into arterial (A; genes *Hey1*, *Bmx*, and *Sema3g*), capillary (C; genes *Slc16a2*, *Car4*, and *Mfsd2a*), and venous (V; genes *Icam1*, *Slc38a5*, and *Vwf*) zonal identities (Figures 4E and S3).[21] Further analysis suggests that the strongest DEGs are shared among zonal identities and include genes involved in antigen presentation, interleukin receptor subunits, and adhesion molecules. Unique DEGs identified in the A and V zonal identities did not show any significant func-

cells (EC_hb), endothelial/stromal cells or pericyte-like cells (ECs/PCs), endothelial/stromal cells or astrocyte-like cells (ECs/ACs), astrocytes (ACs), B cells, T cells, monocytes (MNCs), microglia (MG), oligodendrocytes (OLGs), and fibroblasts (Figure S3). Endothelial cells were the largest represented cell type, followed by immune cells such as monocytes and T cells that are also predicted to express CD31 (Figures 4B and S3); other cell types likely represent some small contamination in the sorting process. Each cell type was annotated using previously established marker genes,[49] and all non-endothelial clusters were filtered out of the dataset for these initial analyses. WT and Iqgap2$^{-/-}$ (KO) genotypes were equally represented in the EC cluster (Figure 4C), and bulk gene expression comparisons between WT and KO BECs show 928 differentially regulated genes (DEGs) (Figure 4D). Since leukocyte extravasation occurs predominantly at post-capillary venules,[50–52] we exam-

tional enrichment, whereas a similar analysis of unique DEGs identified in the C zonal identity suggest subtle changes in BEC function (Figure 4F; Table S1).

Across these zones, we were able to confirm that loss of Iqgap2 does not significantly affect expression of most canonical BBB genes, including junction proteins and nutrient transporters such as *Cdh5*, *Cldn5*, *Ocln*, *Tjp*, and *Slc2a1* (Figure S4A). At the protein level, total vessel density was unchanged, and we observed no obvious deficits in expression of claudin-5, occludin, ZO-1, and Glut1 in the Iqgap2$^{-/-}$ mice (Figure S5). We did observe significant differences in gene expression for certain transporters that facilitate exchange of amino acids and metabolites across the BBB, such as *Abcb1a*, *Slc7a1*, *Slc7a5*, and *Slc16a1* (Figure S4B). In addition, major regulator genes involved in BBB functional development and maintenance like *Mfsd2a*[53] and *Ctnnb1*[54–56] were significantly downregulated in
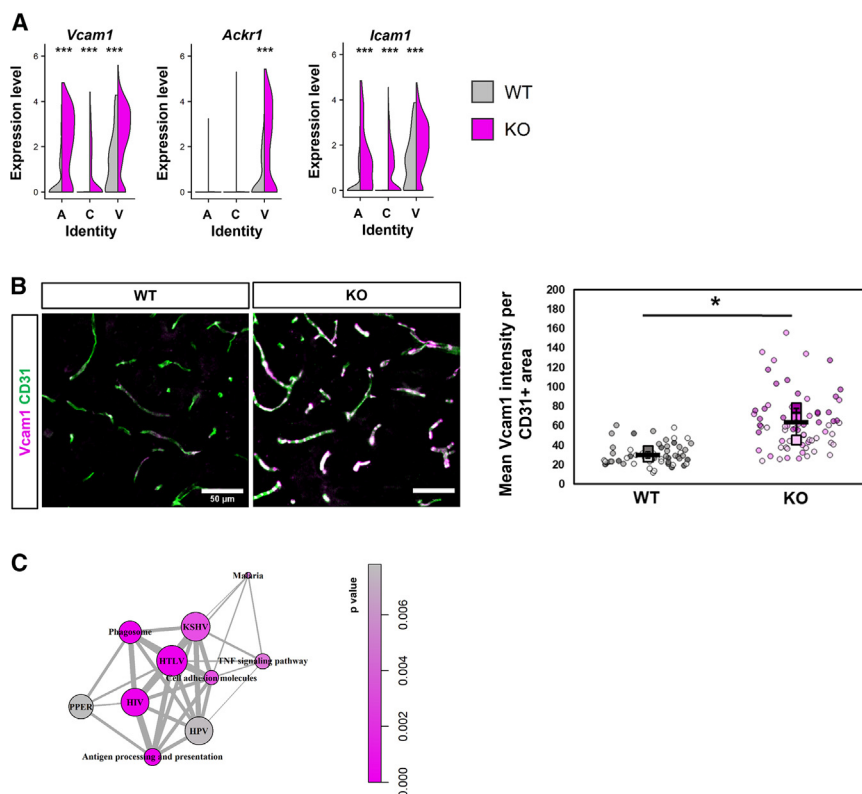
Figure 5. Global loss of Iqgap2 produces a widespread inflammatory phenotype in BECs

(A) Split violin plots indicating differential gene expression of select inflammatory markers across vascular zones between wild-type (WT) and Iqgap2$^{-/-}$ (KO) BECs. Statistical significance was calculated using Wilcox rank-order tests with Bonferroni correction (***$p < 0.001$).

(B) Representative images and quantification of vascular Vcam1 expression in WT versus KO mouse cortex. Scale bars represent 50 μm. Data are represented as mean ± SD (black bars). Biological replicates are represented as squares, and measurements from individual images are represented as circles color coded to each replicate. Quantification was performed across $N = 3$ biological replicates. Statistical significance was calculated using the student's unpaired t test (*$p < 0.05$).

(C) GSEA analysis for signaling pathways upregulated in KO versus WT BECs. Each node represents an enriched gene set belonging to the labeled canonical pathway. Nodes are colored based on p value, and thickness of the connecting lines indicates similarity of overlapping genes represented in connected gene sets. KSHV, Kaposi-sarcoma-associated herpes virus infection; HTLV, human T cell leukemia virus 1 infection; HIV, human immunodeficiency virus 1 infection; PPER, protein processing in endoplasmic reticulum; HPV, human papillomavirus infection.

the Iqgap2$^{-/-}$ BECs, suggesting possible connections to BBB dysfunction (Figure S4C). Interestingly, we also saw significant upregulation of several LAMs and chemokine receptors. Although interaction with leukocytes and response to inflammation are primarily facilitated by venous ECs, we found that loss of Iqgap2 significantly upregulates expression of leukocyte receptors and signaling molecules like *Vcam1*, *Icam1*, and *Ackr1* across multiple vascular zones (Figure 5A). Using immunohistochemistry, we confirmed upregulation of Vcam1 in cortical vasculature of Iqgap2$^{-/-}$ mice (Figure 5B). The widespread expression of vascular Vcam1 in Iqgap2$^{-/-}$ mice was particularly striking, given that Vcam1 expression on BECs has been implicated in brain inflammation and cognitive decline in mice.[57] We have also recently shown that vascular VCAM-1 expression is significantly increased in Alzheimer's disease cortex relative to asymptomatic age-matched controls, further highlighting its links to human neurodegeneration.[58]

To extend our understanding of potential pathways in BECs affected by global loss of Iqgap2, we performed gene set enrichment analysis (GSEA) for KEGG signaling pathways. GSEA indicated that pathways involved in response to infections like Kaposi-sarcoma-associated herpes virus infection (KSHV), human T cell leukemia virus 1 infection (HTLV), human immunodeficiency virus 1 infection (HIV), and human papillomavirus infection (HPV) were upregulated. In addition, other pathways facilitating immune interactions like cell adhesion (*Vcam1*, *Icam1*), antigen processing and presentation (*Psme2*, *Hspa5*, *Canx*, *Calr*), and TNF signaling (*Cxcl1*, *Csf1*, *Ptgs2*) were also significantly upregulated in the Iqgap2$^{-/-}$ BECs (Figures 5C

and S6). These results indicate that *Iqgap2* loss shifts both the transcriptional profile and protein expression of BECs toward an activated, inflammatory state.

Due to the significant upregulation of LAMs in the Iqgap2$^{-/-}$ BECs, we further analyzed cell-cell interactions between BECs and other cell types identified in the scRNA-seq dataset using CellChat.[59] We found that BEC-immune cell interactions were overrepresented in Iqgap2$^{-/-}$ mice. Quantification of these results suggested an increase in cell-cell interactions between BECs and microglia as well as BECs and peripheral immune cells like monocytes, T cells, and B cells. As Iqgap2 is predicted to be expressed in immune cell types,[60] we sought to assess whether loss of Iqgap2 influences resident microglial populations in the mouse brain. We found that there were no significant differences in the number of cortical microglia between the WT and Iqgap2$^{-/-}$ mice (Figure S7A). We also determined there were no significant changes in the microglial morphology profiles of Iqgap2$^{-/-}$ mouse brain cortices (Figure S7B), potentially indicating that microglia are mostly unaffected by loss of Iqgap2. We then assessed the predicted directionality of these interactions by analyzing known receptor-ligand pairs. BECs were predicted to be the "senders," whereas immune populations, especially monocytes, were the primary "receivers" (Figure S8). To understand whether these changes were due to Iqgap2 loss in a specific cell type, we performed DEG analyses in all clusters annotated as immune populations. Monocytes had the highest number of significant DEGs, followed by microglia and T cells (Figure S9A). KEGG pathway analysis of DEGs in the monocytes indicated upregulation of pathways such as
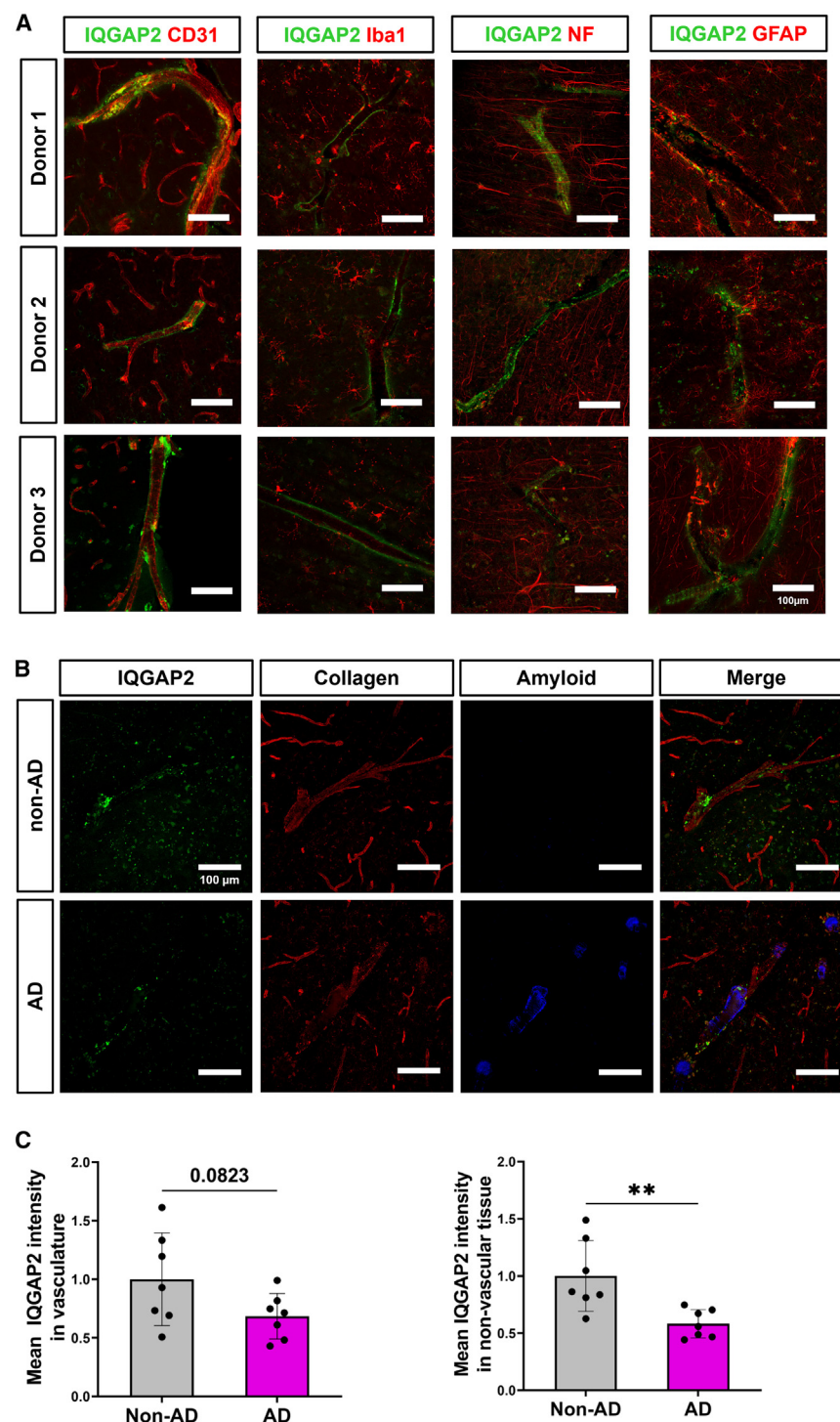
Figure 6. IQGAP2 distribution in human brain tissue

(A) Representative confocal microscopy images of IQGAP2 and different markers for endothelium (CD31), microglia (Iba1), neurons (NF), and astrocytes (GFAP) in superior temporal lobe from donors without neurological disease. $N = 3$ individual donors. Scale bars represent 100 μm.

(B) Representative confocal microscopy images of IQGAP2 (green) in human hippocampal tissue from AD and non-AD donors. Images were produced from 10 μm z stack scanning projections with a step interval of 1 μm. Vasculature was stained with collagen (red) and β-amyloid, and neuritic plaques, neurofibrillary tangles, and other tau aggregates were stained with Methoxy-X04 (blue). Scale bars represent 100 μm.

(C) Mean IQGAP2 intensity in vascular regions was quantified with one scanning projection in collagen+ area, whereas IQGAP2 intensity in parenchyma was quantified by gating samples to exclude collagen+ area. Scale bars represent 100 μm. Data are presented as mean ± SD, where each data point represents an individual donor with at least five images quantified per donor. $N = 7$ non-AD donors and $N = $ AD 7 donors. Statistical significance was calculated using unpaired Student's t test (**$p < 0.01$).

IQGAP2 in postmortem human brain tissue

To putatively assess connections between IQGAP2 and human disease states, we evaluated IQGAP2 protein distribution patterns in postmortem human brain tissue. Using a custom polyclonal antibody raised against a peptide with selective homology to human IQGAP, we co-labeled IQGAP2 with cell-type-specific markers for endothelium (CD31), microglia (Iba), neurons (NF), and astrocytes (GFAP) in superior temporal lobe tissue (Figure 6A). IQGAP2 was primarily detected alongside CD31$^+$ endothelial cells, indicating its association with vascular cells. We also noted astrocytic labeling in some tissue specimens but no clear associations with neurons or microglia, the latter agreeing with the observations in Figure S7. Next, we immunostained and quantified vascular-associated and parenchymal IQGAP2 signal in human hippocampal sections from AD and non-AD patients. IQGAP2 staining was again strongly detected along blood vessels identified by collagen expression, with more diffuse and punctate signal observed in the parenchyma (Figure 6B). A significant decrease in IQGAP2 levels was measured in parenchymal regions in AD patients ($p < 0.01$), whereas the decrease in vascular IQGAP2 signal did not reach significance ($p = 0.08$; Figure 6C). The perivascular IQGAP2 signal could

leukocyte transendothelial migration and regulation of actin cytoskeleton (Figure S9B). These data indicate that Iqgap2 may also play an important role in modulating BEC-monocyte communication, which could additionally contribute to the overall inflammatory phenotype observed in the BECs in Iqgap2$^{-/-}$ mice.

represent border-associated cells that are known to play roles in brain health and immunity,[61,62] highlighting the potential importance of this finding that will be mechanistically explored in future work.

DISCUSSION

Peripheral endothelial cells display high levels of LAMs and can respond swiftly to local and systemic inflammatory cues.[63] This is followed by rapid infiltration of leukocytes into surrounding tissue beds. In comparison, BECs are comparably immune quiescent under homeostatic conditions and generally express low levels of LAMs. This allows the BBB to more selectively control the activation of downstream inflammatory pathways and extravasation of leukocytes into the CNS.[64,65] Although peripheral immune responses are essential for the resolution of CNS injury, it is well established that age-related neurological deficits and chronic neurodegeneration may be exacerbated in part by unwarranted entry of leukocytes into the brain.[39,41,66–68] Further, BECs upregulate transcriptional signatures of inflammatory responses during aging and neurological disease.[24,25,69] As such, identifying mechanisms that regulate BEC inflammatory responses is critical for understanding the pathological progression of these diseases and developing strategies to decrease leukocyte extravasation. Our study provides evidence that IQGAP2 plays an important role in BBB immune dynamics and the propensity of leukocytes to enter the CNS after immune stimulation.

To our knowledge, the role of IQGAP proteins in BBB integrity has not been studied. *IQGAP2* belongs to the *IQGAP* family of scaffolding proteins involved in orchestrating a wide array of intracellular signaling and cytoskeleton dynamics.[29] The multidomain structure of these proteins acts as a framework for complex formation of signaling proteins, thus influencing many downstream cellular processes. *IQGAPs* were historically considered to be modulators of cytoskeletal architecture. However, it has become apparent that their role extends into other physiological processes like glomerular filtration in the kidney, cardiomyocyte function in the heart, smooth muscle cell contraction in lung airways, and metabolism in the liver.[29,70,71] *IQGAP2* has also been studied in the context of its tumor-suppressive characteristics.[72] Previous studies identified *IQGAP2* as a novel tumor suppressor gene specifically linked to the development of hepatocellular carcinoma. More recently, *IQGAP2* inactivation has been linked to other malignancies like gastric cancer,[73] prostate cancer,[74] and bladder cancer.[75] Moreover, reduced expression of *IQGAP2* is associated with worsened cancer pathology and poor clinical outcomes.[74,76,77] Our study provides new context for the role of IQGAP2 in physiological processes related to immune cell trafficking.

An unanswered question is whether changes in IQGAP2 expression contribute to human neurodegenerative disease progression through modulation of immune cell recruitment to the CNS. In the acute and chronic inflammatory animal models used in this study, we did not observe significant differences in pathology. In the EAE model, it is possible that the 30-day time point does not reflect increased damage caused by infiltrating leukocytes due to other compensatory mechanisms (e.g., significant damage could occur at an earlier time point followed by regeneration), especially when

considering the biphasic disease severity in the Iqgap2$^{-/-}$ mice, and that deaths generally occurred during periods where disease severity worsened. In human hippocampal tissue, we observed a decrease in IQGAP2 in patients with AD. In the context of our study, these findings motivate future exploration into whether loss of Iqgap2 influences pathology and immune cell infiltration in mouse and human models of AD.

Overall, our work reveals a novel role for IQGAP2 in regulating BBB immune dynamics. Although the cell-specific effects of IQGAP2 are currently unclear, our collective data suggest that this protein plays an important conserved and previously unrecognized role in suppressing BEC inflammatory responses and regulating immune cell trafficking to the CNS through non-cell autonomous mechanisms. Future work will determine these mechanisms of action and their relevance to brain disorders.

Limitations of the study

One limitation of our study is that we cannot exclusively ascribe the observed CNS leukocyte infiltration to loss of Iqgap2 expression in a particular cell type. *IQGAP2* has generally high expression in many immune cell subtypes,[60] but this has not previously been associated with specific phenotypes like tissue extravasation and responsiveness to inflammatory cytokines. Our current data may suggest that cell-to-cell communication between BECs and immune cells plays a role in BBB inflammation when Iqgap2 is lost. However, more extensive scRNA-seq profiling of the neurovascular unit in Iqgap2$^{-/-}$ mice, as well as lineage-specific Iqgap2 knockout models, will be necessary in future studies to fully clarify cell-intrinsic and cell-extrinsic effects of IQGAP2 on BBB immune privilege.

RESOURCE AVAILABILITY

Lead contact
Further information and requests for resources and reagents should be directed to and will be fulfilled by the lead contact, Ethan Lippmann (ethan.s.lippmann@vanderbilt.edu).

Materials availability
Anti-IQGAP2 antibody generated in this study is available from the lead contact, contingent on sufficient stocks, with a completed materials transfer agreement.

Data and code availability
- The raw scRNA-seq data reported in this study have been deposited at ArrayExpress and are publicly available as of the date of publication. Accession numbers are listed in the key resources table.
- The original code used for scRNA-seq analysis presented in this paper is also publicly available at GitHub. The link to access this code is listed in the key resources table.
- Any additional information required to reanalyze the data reported in this work paper is available from the lead contact upon request.

AUTHOR CONTRIBUTIONS

DECLARATION OF INTERESTS

The authors declare no competing interests.

STAR★METHODS

Detailed methods are provided in the online version of this paper and include the following:

- KEY RESOURCES TABLE
- EXPERIMENTAL MODEL AND STUDY PARTICIPANT DETAILS
  - Human tissue
  - Mice
  - Zebrafish
  - Caco-2 cell line
- METHOD DETAILS
  - Mouse maintenance and procedures
  - Zebrafish maintenance and procedures
  - Human brain tissue preparation
  - Development of a custom antibody against human IQGAP2 protein
  - Caco-2 cell procedures for evaluating human IQGAP2 antibody specificity
  - Immunofluorescent staining
  - Luxol Fast Blue staining
  - Western blotting (mouse tissue)
  - Western blotting (human cells)
  - Single-cell RNA sequencing
  - Single-cell RNA sequencing analysis
- QUANTIFICATION AND STATISTICAL ANALYSIS

SUPPLEMENTAL INFORMATION

Supplemental information can be found online at https://doi.org/10.1016/j.isci.2025.111994.

REFERENCES

1. Profaci, C.P., Munji, R.N., Pulido, R.S., and Daneman, R. (2020). The blood–brain barrier in health and disease: Important unanswered questions. J. Exp. Med. 217, e20190062. https://doi.org/10.1084/jem.20190062.

2. Daneman, R., and Prat, A. (2015). The Blood–Brain Barrier. Cold Spring Harb. Perspect. Biol. 7, a020412. https://doi.org/10.1101/cshperspect.a020412.

3. Obermeier, B., Daneman, R., and Ransohoff, R.M. (2013). Development, maintenance and disruption of the blood-brain barrier. Nat. Med. 19, 1584–1596. https://doi.org/10.1038/nm.3407.

4. Engelhardt, B., and Coisne, C. (2011). Fluids and barriers of the CNS establish immune privilege by confining immune surveillance to a two-walled castle moat surrounding the CNS castle. Fluids Barriers CNS 8, 4. https://doi.org/10.1186/2045-8118-8-4.

5. Louveau, A., Harris, T.H., and Kipnis, J. (2015). Revisiting the Mechanisms of CNS Immune Privilege. Trends Immunol. 36, 569–577. https://doi.org/10.1016/j.it.2015.08.006.

6. Engelhardt, B., Vajkoczy, P., and Weller, R.O. (2017). The movers and shapers in immune privilege of the CNS. Nat. Immunol. 18, 123–131. https://doi.org/10.1038/ni.3666.

7. Marchetti, L., and Engelhardt, B. (2020). Immune cell trafficking across the blood-brain barrier in the absence and presence of neuroinflammation. Vasc. Biol. 2, H1–H18. https://doi.org/10.1530/VB-19-0033.

8. Mapunda, J.A., Tibar, H., Regragui, W., and Engelhardt, B. (2022). How Does the Immune System Enter the Brain? Front. Immunol. 13, 805657. https://doi.org/10.3389/fimmu.2022.805657.

9. Raivich, G. (2005). Like cops on the beat: the active role of resting microglia. Trends Neurosci. 28, 571–573. https://doi.org/10.1016/j.tins.2005.09.001.

10. Ousman, S.S., and Kubes, P. (2012). Immune surveillance in the central nervous system. Nat. Neurosci. 15, 1096–1101. https://doi.org/10.1038/nn.3161.

11. Laman, J.D., and Weller, R.O. (2013). Drainage of Cells and Soluble Antigen from the CNS to Regional Lymph Nodes. J. Neuroimmune Pharmacol. 8, 840–856. https://doi.org/10.1007/s11481-013-9470-8.

12. Louveau, A., Plog, B.A., Antila, S., Alitalo, K., Nedergaard, M., and Kipnis, J. (2017). Understanding the functions and relationships of the glymphatic system and meningeal lymphatics. J. Clin. Investig. 127, 3210–3219. https://doi.org/10.1172/JCI90603.

13. Engelhardt, B., Carare, R.O., Bechmann, I., Flügel, A., Laman, J.D., and Weller, R.O. (2016). Vascular, glial, and lymphatic immune gateways of the central nervous system. Acta Neuropathol. 132, 317–338. https://doi.org/10.1007/s00401-016-1606-5.

14. das Neves, S.P., Delivanoglou, N., and Da Mesquita, S. (2021). CNS-Draining Meningeal Lymphatic Vasculature: Roles, Conundrums and Future Challenges. Front. Pharmacol. 12, 655052. https://doi.org/10.3389/fphar.2021.655052.

15. Engelhardt, B., and Ransohoff, R.M. (2005). The ins and outs of T-lymphocyte trafficking to the CNS: anatomical sites and molecular mechanisms. Trends Immunol. 26, 485–495. https://doi.org/10.1016/j.it.2005.07.004.

16. Engelhardt, B., and Ransohoff, R.M. (2012). Capture, crawl, cross: the T cell code to breach the blood–brain barriers. Trends Immunol. 33, 579–589. https://doi.org/10.1016/j.it.2012.07.004.

17. Aydin, S., Pareja, J., Schallenberg, V.M., Klopstein, A., Gruber, T., Page, N., Bouillet, E., Blanchard, N., Liblau, R., Körbelin, J., et al. (2023). Antigen recognition detains CD8+ T cells at the blood-brain barrier and contributes to its breakdown. Nat. Commun. 14, 3106. https://doi.org/10.1038/s41467-023-38703-2.

18. Fain, C.E., Zheng, J., Jin, F., Ayasoufi, K., Wu, Y., Lilley, M.T., Dropik, A.R., Wolf, D.M., Rodriguez, R.C., Aibaidula, A., et al. (2024). Discrete class I

molecules on brain endothelium differentially regulate neuropathology in experimental cerebral malaria. Brain *147*, 566–589. https://doi.org/10.1093/brain/awad319.

19. Lopes Pinheiro, M.A., Kamermans, A., Garcia-Vallejo, J.J., van het Hof, B., Wierts, L., O'Toole, T., Boeve, D., Verstege, M., van der Pol, S.M., van Kooyk, Y., et al. (2016). Internalization and presentation of myelin antigens by the brain endothelium guides antigen-specific T cell migration. Elife *5*, e13149. https://doi.org/10.7554/eLife.13149.

20. Galea, I. (2021). The blood–brain barrier in systemic infection and inflammation. Cell. Mol. Immunol. *18*, 2489–2501. https://doi.org/10.1038/s41423-021-00757-x.

21. Vanlandewijck, M., He, L., Mäe, M.A., Andrae, J., Ando, K., Del Gaudio, F., Nahar, K., Lebouvier, T., Laviña, B., Gouveia, L., et al. (2018). A molecular atlas of cell types and zonation in the brain vasculature. Nature *554*, 475–480. https://doi.org/10.1038/nature25739.

22. Sabbagh, M.F., Heng, J.S., Luo, C., Castanon, R.G., Nery, J.R., Rattner, A., Goff, L.A., Ecker, J.R., and Nathans, J. (2018). Transcriptional and epigenomic landscapes of CNS and non-CNS vascular endothelial cells. Elife *7*, e36187. https://doi.org/10.7554/eLife.36187.

23. Kalucka, J., de Rooij, L.P.M.H., Goveia, J., Rohlenova, K., Dumas, S.J., Meta, E., Conchinha, N.V., Taverna, F., Teuwen, L.-A., Veys, K., et al. (2020). Single-Cell Transcriptome Atlas of Murine Endothelial Cells. Cell *180*, 764–779.e20. https://doi.org/10.1016/j.cell.2020.01.015.

24. Yang, A.C., Vest, R.T., Kern, F., Lee, D.P., Agam, M., Maat, C.A., Losada, P.M., Chen, M.B., Schaum, N., Khoury, N., et al. (2022). A human brain vascular atlas reveals diverse mediators of Alzheimer's risk. Nature *603*, 885–892. https://doi.org/10.1038/s41586-021-04369-3.

25. Garcia, F.J., Sun, N., Lee, H., Godlewski, B., Mathys, H., Galani, K., Zhou, B., Jiang, X., Ng, A.P., Mantero, J., et al. (2022). Single-cell dissection of the human brain vasculature. Nature *603*, 893–899. https://doi.org/10.1038/s41586-022-04521-7.

26. Winkler, E.A., Kim, C.N., Ross, J.M., Garcia, J.H., Gil, E., Oh, I., Chen, L.Q., Wu, D., Catapano, J.S., Raygor, K., et al. (2022). A single-cell atlas of the normal and malformed human brain vasculature. Science *375*, eabi7377. https://doi.org/10.1126/science.abi7377.

27. Sullivan, D.P., Dalal, P.J., Jaulin, F., Sacks, D.B., Kreitzer, G., and Muller, W.A. (2019). Endothelial IQGAP1 regulates leukocyte transmigration by directing the LBRC to the site of diapedesis. J. Exp. Med. *216*, 2582–2601. https://doi.org/10.1084/jem.20190008.

28. Sullivan, D.P., Dalal, P.J., Sacks, D.B., and Muller, W.A. (2020). Calcium Signaling Regulates Leukocyte Transendothelial Migration through the Action of Endothelial Cell IQGAP1, Calmodulin, and CaMKIIδ. FASEB J. *34*, 1. https://doi.org/10.1096/fasebj.2020.34.s1.05149.

29. Smith, J.M., Hedman, A.C., and Sacks, D.B. (2015). IQGAPs choreograph cellular signaling from the membrane to the nucleus. Trends Cell Biol. *25*, 171–184. https://doi.org/10.1016/j.tcb.2014.12.005.

30. Dai, Q., Ain, Q., Rooney, M., Song, F., and Zipprich, A. (2022). Role of IQ Motif-Containing GTPase-Activating Proteins in Hepatocellular Carcinoma. Front. Oncol. *12*, 920652. https://doi.org/10.3389/fonc.2022.920652.

31. Jin, X., Liu, Y., Liu, J., Lu, W., Liang, Z., Zhang, D., Liu, G., Zhu, H., Xu, N., and Liang, S. (2015). The Overexpression of IQGAP1 and β-Catenin Is Associated with Tumor Progression in Hepatocellular Carcinoma In Vitro and In Vivo. PLoS One *10*, e0133770. https://doi.org/10.1371/journal.pone.0133770.

32. White, C.D., Khurana, H., Gnatenko, D.V., Li, Z., Odze, R.D., Sacks, D.B., and Schmidt, V.A. (2010). IQGAP1 and IQGAP2 are Reciprocally Altered in Hepatocellular Carcinoma. BMC Gastroenterol. *10*, 125. https://doi.org/10.1186/1471-230X-10-125.

33. Schmidt, V.A., Chiariello, C.S., Capilla, E., Miller, F., and Bahou, W.F. (2008). Development of Hepatocellular Carcinoma in *Iqgap2* -Deficient Mice Is IQGAP1 Dependent. Mol. Cell Biol. *28*, 1489–1502. https://doi.org/10.1128/MCB.01090-07.

34. Zhang, Y., Chen, K., Sloan, S.A., Bennett, M.L., Scholze, A.R., O'Keeffe, S., Phatnani, H.P., Guarnieri, P., Caneda, C., Ruderisch, N., et al. (2014). An RNA-Sequencing Transcriptome and Splicing Database of Glia, Neurons, and Vascular Cells of the Cerebral Cortex. J. Neurosci. *34*, 11929–11947. https://doi.org/10.1523/JNEUROSCI.1860-14.2014.

35. Zhang, Y., Sloan, S.A., Clarke, L.E., Caneda, C., Plaza, C.A., Blumenthal, P.D., Vogel, H., Steinberg, G.K., Edwards, M.S.B., Li, G., et al. (2016). Purification and Characterization of Progenitor and Mature Human Astrocytes Reveals Transcriptional and Functional Differences with Mouse. Neuron *89*, 37–53. https://doi.org/10.1016/j.neuron.2015.11.013.

36. He, L., Vanlandewijck, M., Mäe, M.A., Andrae, J., Ando, K., Del Gaudio, F., Nahar, K., Lebouvier, T., Laviña, B., Gouveia, L., et al. (2018). Single-cell RNA sequencing of mouse brain and lung vascular and vessel-associated cell types. Sci. Data *5*, 180160. https://doi.org/10.1038/sdata.2018.160.

37. Proescholdt, M.G., Chakravarty, S., Foster, J.A., Foti, S.B., Briley, E.M., and Herkenham, M. (2002). Intracerebroventricular but not intravenous interleukin-1β induces widespread vascular-mediated leukocyte infiltration and immune signal mRNA expression followed by brain-wide glial activation. Neuroscience *112*, 731–749. https://doi.org/10.1016/S0306-4522(02)00048-9.

38. Liu, X., Nemeth, D.P., McKim, D.B., Zhu, L., DiSabato, D.J., Berdysz, O., Gorantla, G., Oliver, B., Witcher, K.G., Wang, Y., et al. (2019). Cell-Type-Specific Interleukin 1 Receptor 1 Signaling in the Brain Regulates Distinct Neuroimmune Activities. Immunity *50*, 764–766. https://doi.org/10.1016/j.immuni.2019.02.012.

39. Amor, S., Puentes, F., Baker, D., and van der Valk, P. (2010). Inflammation in neurodegenerative diseases. Immunology *129*, 154–169. https://doi.org/10.1111/j.1365-2567.2009.03225.x.

40. Gate, D., Tapp, E., Leventhal, O., Shahid, M., Nonninger, T.J., Yang, A.C., Strempfl, K., Unger, M.S., Fehlmann, T., Oh, H., et al. (2021). CD4 + T cells contribute to neurodegeneration in Lewy body dementia. Science *374*, 868–874. https://doi.org/10.1126/science.abf7266.

41. Gate, D., Saligrama, N., Leventhal, O., Yang, A.C., Unger, M.S., Middeldorp, J., Chen, K., Lehallier, B., Channappa, D., De Los Santos, M.B., et al. (2020). Clonally expanded CD8 T cells patrol the cerebrospinal fluid in Alzheimer's disease. Nature *577*, 399–404. https://doi.org/10.1038/s41586-019-1895-7.

42. Unger, M.S., Li, E., Scharnagl, L., Poupardin, R., Altendorfer, B., Mrowetz, H., Hutter-Paier, B., Weiger, T.M., Heneka, M.T., Attems, J., and Aigner, L. (2020). CD8+ T-cells infiltrate Alzheimer's disease brains and regulate neuronal- and synapse-related gene expression in APP-PS1 transgenic mice. Brain Behav. Immun. *89*, 67–86. https://doi.org/10.1016/j.bbi.2020.05.070.

43. Earls, R.H., and Lee, J.-K. (2020). The role of natural killer cells in Parkinson's disease. Exp. Mol. Med. *52*, 1517–1525. https://doi.org/10.1038/s12276-020-00505-7.

44. Hemmer, B., Kerschensteiner, M., and Korn, T. (2015). Role of the innate and adaptive immune responses in the course of multiple sclerosis. Lancet Neurol. *14*, 406–419. https://doi.org/10.1016/S1474-4422(14)70305-9.

45. Stephenson, J., Nutma, E., Van Der Valk, P., and Amor, S. (2018). Inflammation in CNS neurodegenerative diseases. Immunology *154*, 204–219. https://doi.org/10.1111/imm.12922.

46. Constantinescu, C.S., Farooqi, N., O'Brien, K., and Gran, B. (2011). Experimental autoimmune encephalomyelitis (EAE) as a model for multiple sclerosis (MS). Br. J. Pharmacol. *164*, 1079–1106. https://doi.org/10.1111/j.1476-5381.2011.01302.x.

47. O'Brown, N.M., Megason, S.G., and Gu, C. (2019). Suppression of transcytosis regulates zebrafish blood-brain barrier function. Elife *8*, e47326. https://doi.org/10.7554/eLife.47326.

48. Shiau, C.E., Monk, K.R., Joo, W., and Talbot, W.S. (2013). An Anti-inflammatory NOD-like Receptor Is Required for Microglia Development. Cell Rep. *5*, 1342–1352. https://doi.org/10.1016/j.celrep.2013.11.004.

49. Zhao, L., Li, Z., Vong, J.S.L., Chen, X., Lai, H.-M., Yan, L.Y.C., Huang, J., Sy, S.K.H., Tian, X., Huang, Y., et al. (2020). Pharmacologically reversible zonation-dependent endothelial cell transcriptomic changes with neuro-degenerative disease associations in the aged brain. Nat. Commun. 11, 4413. https://doi.org/10.1038/s41467-020-18249-3.

50. Rossi, B., Angiari, S., Zenaro, E., Budui, S.L., and Constantin, G. (2011). Vascular inflammation in central nervous system diseases: adhesion receptors controlling leukocyte-endothelial interactions. J. Leukoc. Biol. 89, 539–556. https://doi.org/10.1189/jlb.0710432.

51. Muller, W.A. (2013). Getting Leukocytes to the Site of Inflammation. Vet. Pathol. 50, 7–22. https://doi.org/10.1177/0300985812469883.

52. Nourshargh, S., and Alon, R. (2014). Leukocyte Migration into Inflamed Tissues. Immunity 41, 694–707. https://doi.org/10.1016/j.immuni.2014.10.008.

53. Ben-Zvi, A., Lacoste, B., Kur, E., Andreone, B.J., Mayshar, Y., Yan, H., and Gu, C. (2014). Mfsd2a is critical for the formation and function of the blood–brain barrier. Nature 509, 507–511. https://doi.org/10.1038/nature13324.

54. Daneman, R., Agalliu, D., Zhou, L., Kuhnert, F., Kuo, C.J., and Barres, B.A. (2009). Wnt/β-catenin signaling is required for CNS, but not non-CNS, angiogenesis. Proc. Natl. Acad. Sci. USA 106, 641–646. https://doi.org/10.1073/pnas.0805165106.

55. Stenman, J.M., Rajagopal, J., Carroll, T.J., Ishibashi, M., McMahon, J., and McMahon, A.P. (2008). Canonical Wnt Signaling Regulates Organ-Specific Assembly and Differentiation of CNS Vasculature. Science 322, 1247–1250. https://doi.org/10.1126/science.1164594.

56. Liebner, S., Corada, M., Bangsow, T., Babbage, J., Taddei, A., Czupalla, C.J., Reis, M., Felici, A., Wolburg, H., Fruttiger, M., et al. (2008). Wnt/β-catenin signaling controls development of the blood–brain barrier. J. Cell Biol. 183, 409–417. https://doi.org/10.1083/jcb.200806024.

57. Yousef, H., Czupalla, C.J., Lee, D., Chen, M.B., Burke, A.N., Zera, K.A., Zandstra, J., Berber, E., Lehallier, B., Mathur, V., et al. (2019). Aged blood impairs hippocampal neural precursor activity and activates microglia via brain endothelial cell VCAM1. Nat. Med. 25, 988–1000. https://doi.org/10.1038/s41591-019-0440-4.

58. Kim, H., Leng, K., Park, J., Sorets, A.G., Kim, S., Shostak, A., Embalabala, R.J., Mlouk, K., Katdare, K.A., Rose, I.V.L., et al. (2022). Reactive astrocytes transduce inflammation in a blood-brain barrier model through a TNF-STAT3 signaling axis and secretion of alpha 1-antichymotrypsin. Nat. Commun. 13, 6581. https://doi.org/10.1038/s41467-022-34412-4.

59. Jin, S., Guerrero-Juarez, C.F., Zhang, L., Chang, I., Ramos, R., Kuan, C.-H., Myung, P., Plikus, M.V., and Nie, Q. (2021). Inference and analysis of cell-cell communication using CellChat. Nat. Commun. 12, 1088. https://doi.org/10.1038/s41467-021-21246-9.

60. Uhlén, M., Fagerberg, L., Hallström, B.M., Lindskog, C., Oksvold, P., Mardinoglu, A., Sivertsson, Å., Kampf, C., Sjöstedt, E., Asplund, A., et al. (2015). Tissue-based map of the human proteome. Science 347, 1260419. https://doi.org/10.1126/science.1260419.

61. Mason, H.D., and McGavern, D.B. (2022). How the immune system shapes neurodegenerative diseases. Trends Neurosci. 45, 733–748. https://doi.org/10.1016/j.tins.2022.08.001.

62. Hammond, T.R., Marsh, S.E., and Stevens, B. (2019). Immune Signaling in Neurodegeneration. Immunity 50, 955–974. https://doi.org/10.1016/j.immuni.2019.03.016.

63. Bevilacqua, M.P. (1993). Endothelial-Leukocyte Adhesion Molecules. Annu. Rev. Immunol. 11, 767–804. https://doi.org/10.1146/annurev.iy.11.040193.004003.

64. Hickey, W.F., Hsu, B.L., and Kimura, H. (1991). T-lymphocyte entry into the central nervous system. J. Neurosci. Res. 28, 254–260. https://doi.org/10.1002/jnr.490280213.

65. Rössler, K., Neuchrist, C., Kitz, K., Scheiner, O., Kraft, D., and Lassmann, H. (1992). Expression of leucocyte adhesion molecules at the human blood-brain barrier (BBB). J. Neurosci. Res. 31, 365–374. https://doi.org/10.1002/jnr.490310219.

66. Yilmaz, G., and Granger, D.N. (2008). Cell adhesion molecules and ischemic stroke. Neurol. Res. 30, 783–793. https://doi.org/10.1179/174313208X341085.

67. Roberts, T.K., Buckner, C.M., and Berman, J.W. (2010). Leukocyte transmigration across the blood-brain barrier: perspectives on neuroAIDS. Front. Biosci. 15, 478–536. https://doi.org/10.2741/3631.

68. Dulken, B.W., Buckley, M.T., Navarro Negredo, P., Saligrama, N., Cayrol, R., Leeman, D.S., George, B.M., Boutet, S.C., Hebestreit, K., Pluvinage, J.V., et al. (2019). Single-cell analysis reveals T cell infiltration in old neurogenic niches. Nature 571, 205–210. https://doi.org/10.1038/s41586-019-1362-5.

69. Chen, M.B., Yang, A.C., Yousef, H., Lee, D., Chen, W., Schaum, N., Lehallier, B., Quake, S.R., and Wyss-Coray, T. (2020). Brain Endothelial Cells Are Exquisite Sensors of Age-Related Circulatory Cues. Cell Rep. 30, 4418–4432.e4. https://doi.org/10.1016/j.celrep.2020.03.012.

70. Hedman, A.C., Smith, J.M., and Sacks, D.B. (2015). The biology of IQGAP proteins: beyond the cytoskeleton. EMBO Rep. 16, 427–446. https://doi.org/10.15252/embr.201439834.

71. Sen, A., Youssef, S., Wendt, K., and Anakk, S. (2023). Depletion of IQ motif-containing GTPase activating protein 2 (IQGAP2) reduces hepatic glycogen and impairs insulin signaling. J. Biol. Chem. 299, 105322. https://doi.org/10.1016/j.jbc.2023.105322.

72. Xie, Y., Kapoor, A., Peng, H., Cutz, J.-C., Tao, L., and Tang, D. (2015). IQGAP2 Displays Tumor Suppression Functions. J. Anal. Oncol. 4, 86–93. https://doi.org/10.6000/1927-7229.2015.04.02.5.

73. Xu, L., Shao, Y., Ren, L., Liu, X., Li, Y., Xu, J., and Ye, Y. (2020). IQGAP2 Inhibits Migration and Invasion of Gastric Cancer Cells via Elevating SHIP2 Phosphatase Activity. Int. J. Mol. Sci. 21, 1968. https://doi.org/10.3390/ijms21061968.

74. Xie, Y., Zheng, L., and Tao, L. (2019). Downregulation of IQGAP2 Correlates with Prostate Cancer Recurrence and Metastasis. Transl. Oncol. 12, 236–244. https://doi.org/10.1016/j.tranon.2018.10.009.

75. Song, F., Kotolloshi, R., Gajda, M., Hölzer, M., Grimm, M.-O., and Steinbach, D. (2022). Reduced IQGAP2 Promotes Bladder Cancer through Regulation of MAPK/ERK Pathway and Cytokines. Int. J. Mol. Sci. 23, 13508. https://doi.org/10.3390/ijms232113508.

76. Dai, Q., Song, F., Li, X., Huang, F., and Zhao, H. (2022). Comprehensive analysis of the expression and prognosis for IQ motif-containing GTPase-activating proteins in hepatocellular carcinoma. BMC Cancer 22, 1121. https://doi.org/10.1186/s12885-022-10204-3.

77. Deng, Z., Wang, L., Hou, H., Zhou, J., and Li, X. (2016). Epigenetic regulation of IQGAP2 promotes ovarian cancer progression via activating Wnt/β-catenin signaling. Int. J. Oncol. 48, 153–160. https://doi.org/10.3892/ijo.2015.3228.

78. Chi, N.C., Shaw, R.M., De Val, S., Kang, G., Jan, L.Y., Black, B.L., and Stainier, D.Y.R. (2008). Foxn4 directly regulates tbx2b expression and atrioventricular canal formation. Genes Dev. 22, 734–739. https://doi.org/10.1101/gad.1629408.

79. Ellett, F., Pase, L., Hayman, J.W., Andrianopoulos, A., and Lieschke, G.J. (2011). mpeg1 promoter transgenes direct macrophage-lineage expression in zebrafish. Blood 117, e49–e56. https://doi.org/10.1182/blood-2010-10-314120.

80. Stuart, T., Butler, A., Hoffman, P., Hafemeister, C., Papalexi, E., Mauck, W.M., Hao, Y., Stoeckius, M., Smibert, P., and Satija, R. (2019). Comprehensive Integration of Single-Cell Data. Cell 177, 1888–1902.e21. https://doi.org/10.1016/j.cell.2019.05.031.

81. Romero-Fernandez, W., Carvajal-Tapia, C., Prusky, A., Katdare, K.A., Wang, E., Shostak, A., Ventura-Antunes, L., Harmsen, H.J., Lippmann, E.S., Fuxe, K., et al. (2023). Detection, visualization and quantification of protein complexes in human Alzheimer's disease brains using proximity ligation assay. Sci. Rep. 13, 11948. https://doi.org/10.1038/s41598-023-38000-4.

82. Westerfield, M. (2000). The zebrafish book. A guide for the laboratory use of zebrafish (Danio rerio), 4th ed. (Univ. of Oregon Press, Eugene).

83. Lee, Y.-K., Uchida, H., Smith, H., Ito, A., and Sanchez, T. (2019). The isolation and molecular characterization of cerebral microvessels. Nat. Protoc. 14, 3059–3081. https://doi.org/10.1038/s41596-019-0212-0.

84. Davis, B.M., Salinas-Navarro, M., Cordeiro, M.F., Moons, L., and De Groef, L. (2017). Characterizing microglia activation: a spatial statistics approach to maximize information extraction. Sci. Rep. 7, 1576. https://doi.org/10.1038/s41598-017-01747-8.

85. Kim, J., Pavlidis, P., and Ciernia, A.V. (2023). Development of a high-throughput pipeline to characterize microglia morphological states at a single-cell resolution. eNeuro 11, 1576, ENEURO.0014-24.2024. https://doi.org/10.1101/2023.11.03.565581.

86. Romero-Fernandez, W., Borroto-Escuela, D.O., Vargas-Barroso, V., Narváez, M., Di Palma, M., Agnati, L.F., Larriva Sahd, J., and Fuxe, K. (2014). Dopamine D1 and D2 receptor immunoreactivities in the arcuate-median eminence complex and their link to the tubero-infundibular dopamine neurons. Eur. J. Histochem. 58, 2400. https://doi.org/10.4081/ejh.2014.2400.

87. Nackenoff, A.G., Hohman, T.J., Neuner, S.M., Akers, C.S., Weitzel, N.C., Shostak, A., Ferguson, S.M., Mobley, B., Bennett, D.A., Schneider, J.A., et al. (2021). PLD3 is a neuronal lysosomal phospholipase D associated with β-amyloid plaques and cognitive function in Alzheimer's disease. PLoS Genet. 17, e1009406. https://doi.org/10.1371/journal.pgen.1009406.

88. Becht, E., McInnes, L., Healy, J., Dutertre, C.-A., Kwok, I.W.H., Ng, L.G., Ginhoux, F., and Newell, E.W. (2018). Dimensionality reduction for visualizing single-cell data using UMAP. Nat. Biotechnol. 37, 38–44. https://doi.org/10.1038/nbt.4314.

89. McGinnis, C.S., Murrow, L.M., and Gartner, Z.J. (2019). DoubletFinder: Doublet Detection in Single-Cell RNA Sequencing Data Using Artificial Nearest Neighbors. Cell Syst. 8, 329–337.e4. https://doi.org/10.1016/j.cels.2019.03.003.

90. Aran, D., Looney, A.P., Liu, L., Wu, E., Fong, V., Hsu, A., Chak, S., Naikawadi, R.P., Wolters, P.J., Abate, A.R., et al. (2019). Reference-based analysis of lung single-cell sequencing reveals a transitional profibrotic macrophage. Nat. Immunol. 20, 163–172. https://doi.org/10.1038/s41590-018-0276-y.

91. Liao, Y., Wang, J., Jaehnig, E.J., Shi, Z., and Zhang, B. (2019). WebGestalt 2019: gene set analysis toolkit with revamped UIs and APIs. Nucleic Acids Res. 47, W199–W205. https://doi.org/10.1093/nar/gkz401.

92. Blighe, K., Rana, S., and Lewis, M. (2019). EnhancedVolcano: publication-ready volcano plots with enhanced colouring and labeling, 10.18129 R package version 1. https://doi.org/10.18129/B9.bioc.EnhancedVolcano.

93. Lex, A., Gehlenborg, N., Strobelt, H., Vuillemot, R., and Pfister, H. (2014). UpSet: Visualization of Intersecting Sets. IEEE Trans. Vis. Comput. Graph. 20, 1983–1992. https://doi.org/10.1109/TVCG.2014.2346248.

94. Csardi, G., and Nepusz, T. (2006). The igraph software package for complex network research (InterJournal Complex Systems), p. 1695.

STAR★METHODS

KEY RESOURCES TABLE

REAGENT or RESOURCE	SOURCE	IDENTIFIER
Antibodies		
Collagen	DSHB	Cat #: M3F5
IQGAP2	Vanderbilt Antibody and Protein Resource	–
Iqgap2	Santa Cruz Biotechnology	Cat #: sc-55525; RRID: AB_2264816
GAPDH (D16H11)	Cell Signaling Technologies	Cat #: 5174; RRID: AB_10622025
Vcam1	Santa Cruz	Cat #:sc-13160; RRID: AB_626846
CD31 (MEC 13.3)	BD Biosciences	Cat #:553370; RRID: AB_394816
CD45 (30-F11)	BD Biosciences	Cat #: 550539; RRID: AB_2174426
Claudin-5-488	Invitrogen	Cat #: 352588; RRID: AB_2532189
Occludin-594	Invitrogen	Cat #: 331594; RRID: AB_2532186
ZO1-594	Invitrogen	Cat #: 339194; RRID: AB_2532188
GLUT1-488	Abcam	Cat #: ab195359; RRID: AB_2714026
Iba-1	Wako	Cat #: 019-19741; RRID: AB_839504
CD31	R&D Systems	Cat #: AF806; RRID: AB_355617
Neurofilament	Biolegend	Cat #: 837801; RRID: AB_2565383
Iba-1	Aves Labs	Cat #: IBA1-0100; RRID: AB_2910556
GFAP	Abcam	Cat #: ab279291
IRDye® 800CW Goat anti-Rabbit IgG Secondary Antibody	LI-COR	Cat #: 926-32211; RRID: AB_621843
Goat anti-Rat IgG (H + L) Cross-Adsorbed Secondary Antibody, Alexa Fluor™ 647	Invitrogen	Cat #: A21247; RRID: AB_141778
Goat anti-Rat IgG (H + L) Cross-Adsorbed Secondary Antibody, Alexa Fluor™ 488	Invitrogen	Cat #: A11006; RRID: AB_2534074
Goat anti-Chicken IgY (H + L) Secondary Antibody, Alexa Fluor™ 647	Invitrogen	Cat #: A21449; RRID: AB_2535866
Donkey anti-Rabbit IgG (H + L) Highly Cross-Adsorbed Secondary Antibody, Alexa Fluor™ 488	Invitrogen	Cat #: A21206; RRID: AB_2535792
Donkey anti-Rabbit IgG (H + L) Highly Cross-Adsorbed Secondary Antibody, Alexa Fluor™ 555	Invitrogen	Cat #: A31572; RRID: AB_162543
Donkey anti-Mouse IgG (H + L) Highly Cross-Adsorbed Secondary Antibody, Alexa Fluor™ 488	Invitrogen	Cat #: A21202; RRID: AB_141607
Donkey Anti-Rabbit IgG H&L (Alexa Fluor® 488)	Abcam	Cat #: ab150073; RRID: AB_2636877
Donkey Anti-Mouse IgG H&L (Alexa Fluor® 594)	Abcam	Cat #: ab150108; RRID: AB_2732073
Donkey Anti-Rat IgG H&L (Alexa Fluor® 594)	Abcam	Cat #: ab150156; RRID: AB_2890252
Donkey Anti-Sheep IgG H&L (Alexa Fluor® 594)	Abcam	Cat #: ab150180; RRID: AB_2716768
Lycopersicon Esculentum (Tomato) Lectin (LEL, TL), DyLight® 488	Vector Labs	DL-1174-1
Lycopersicon Esculentum (Tomato) Lectin (LEL, TL), DyLight® 649	Vector Labs	DL-1178-1
Biological samples		
AD and non-AD human brain tissue samples	Vanderbilt Brain and Biospecimen Bank at Vanderbilt University Medical Center	IRB Project 180287

(Continued on next page)

Continued

REAGENT or RESOURCE	SOURCE	IDENTIFIER
Chemicals, peptides, and recombinant proteins		
Recombinant murine IL1-β	Peprotech	211-11B
Phosphate Buffered Saline	Thermo Fisher Scientific	10010023
Hooke Kits™ for EAE Induction	Hooke Laboratories	EK-2110
Paraformaldehyde Solution, 4% in PBS	Thermo Scientific Chemicals	J19943.K2
Neutral Red dye	Millipore Sigma	N7005
Critical commercial assays		
Luxol Fast Blue Stain Kit (Myelin Stain)	Abcam	ab150675
Adult Brain Dissociation Kit	Miltenyi Biotec	130-107-677
Deposited data		
Raw sc-RNAseq data	This paper	ArrayExpress: E-MTAB-12687
Github code		
Github code for scRNA-seq data analysis	This paper	https://github.com/LippmannLab/IQGAP2_WT_KO_BEC_scRNAseq
Experimental models: Organisms/strains		
Tg(kdrl:HRAS-mCherry)^{s896}	Chi et al.[78]	
Tg(mpeg1:EGFP)^{gl22}	Ellett et al.[79]	
AB wildtype	Zebrafish International Resource Center	ZL1
129S-*Iqgap2^{tm1Vs}*/J	The Jackson Laboratory	025452
Oligonucleotides		
Primers for Figure S9, see Table S5	This paper	
Single guide RNAs for Figure 3, see Table S5	This paper	
Software and algorithms		
R	The R Foundation	R version 4.1.2
Cell Ranger pipeline	10X Genomics	
Seurat	Stuart et al.[80]	Seurat_4.1.1
CellChat	Jin et al.[59]	CellChat_1.5.0
ImageJ	NIH	ImageJ 1.53e
Image Studio Lite	LICOR	Image Studio Lite 5.2.5
GraphPad Prism	GraphPad Software LLC	GraphPad Prism 9.0.0 and 10.4.0

EXPERIMENTAL MODEL AND STUDY PARTICIPANT DETAILS

Human tissue

Human brain tissue was obtained at autopsy and prepared as previously described.[81] De-identified brain tissue was obtained from the Vanderbilt Brain and Biospecimen Bank at Vanderbilt University Medical Center. Written informed consent for brain donation was obtained from patients or their surrogate decision makers. All brain tissue collection was authorized by the Institutional Review Board at Vanderbilt University Medical Center. Demographics and neuropathological information for each donor are listed in Table S2.

Mice

All mouse protocols were approved by the Institutional Animal Care and Use Committee at Vanderbilt University. Iqgap2$^{-/-}$ mice (129S background) were obtained from Jackson Laboratory (strain 025452). Male and female Iqgap2$^{-/-}$ mice and wildtype littermate controls were used for all experiments. Mice were at least 8 weeks of age at the time of use and were housed continuously in an environmentally controlled facility in a 12-h light/dark cycle with *ad libitum* access to food and water.

Zebrafish

Zebrafish were maintained at 28.5°C following standard protocols.[82] All zebrafish work was approved by the Harvard Medical Area Standing Committee on Animals under protocol number IS00001263-3. Adult fish were maintained on a standard light-dark cycle from 8 a.m. to 10 p.m. Adult fish, aged 3 months to 1.5 years, were crossed to produce embryos and larvae.

Caco-2 cell line

Caco-2 cells were grown in EMEM (Gibco) supplemented with 10% (v/v) fetal bovine serum (Corning) and 100 μg/mL Normocin (InvivoGen) at 37°C in a humidified atmosphere of 5% CO_2 in 6 well plates.

METHOD DETAILS

Mouse maintenance and procedures
Genotyping
Mice were ear-tagged and tail snips were collected at approximately 2 weeks of age. Genomic DNA was extracted using an Extracta DNA Prep kit for tissue (Quantabio) per manufacturer instructions. DNA was extracted in the Extraction buffer at 95°C for 30 min, cooled to room temperature and mixed with Stabilization buffer before being stored at −20°C. The reactions were performed using the Apex Hot Start Taq BLUE Master Mix (Apex Bioresearch) on a ProFlex PCR system (Applied Biosystems). A touchdown cycling protocol was used with an initial annealing temperature of 65°C gradually lowered to 60°C over the course of 10 cycles. Genotyping primers are as follows: Mutant Reverse–ATTTGTCACGTCCTGCACGACG, Wildtype Reverse–TGGCCTTCCTCCCTTAAAGT, and Common Forward–TGACTCAGAGGGCACATGGT. PCR products were run on a 2% agarose-TAE buffered gel supplemented with SYBR Safe DNA Gel Stain (Invitrogen) and imaged using an LI-COR Odyssey Fc gel imager (Figure S10).

Tissue collection
Mice were deeply anesthetized using high-dose isoflurane and euthanized by transcardial perfusion of 1X DPBS (Gibco), followed by 4% paraformaldehyde (PFA, Thermo Fisher Scientific). Brains and lumbar segment of spinal cords were extracted and postfixed in 4% PFA overnight followed by cryopreservation in sucrose gradient solutions (15% and 30%, respectively). The tissue was then embedded in OCT medium (Tissue-Tek) and 15 μm (brain) and 25 μm (spinal cord) thick sections were cut and stored at −80°C.

Microvessel isolation
Mice were deeply anesthetized using high-dose isoflurane and euthanized by decapitation. Brains were extracted and collected in ice-cold PBS. Microvessels from the cortex were isolated as previously described.[83] In brief, cortices were dissected from remaining brain tissue, homogenized in PBS using a tissue homogenizer (Wheaton), and collected by centrifugation. Homogenized tissue was resuspended in a 15% dextran solution (∼70,000 kDa, Sigma) and centrifuged at 10,000xg to separate the vessel fraction from the remaining tissue. The vessel fraction was washed with PBS and filtered using a 40 μm cell strainer (Corning). For protein extraction, the vessel fraction was incubated in RIPA buffer (Sigma) supplemented with 1% v/v protease and phosphatase inhibitor cocktails (Sigma) for 30–60 min on ice. Cell debris was separated by centrifugation (12,000xg for 15 min at 4°C) and the supernatant was stored at −20°C. Protein concentration was quantified using a Pierce BCA Protein Assay (Thermo Fisher Scientific) according to the manufacturer instructions. For immunohistochemical analysis, microvessel suspension was placed on glass slides and allowed to dry at room temperature. Dried microvessels were then fixed with 4% parafolmaldehyde solution and labeled with Lectin DyLight 488 for 30 min at room temperature before mounting in Prolong Gold Antifade Mountant (Invitrogen).

Intracerebroventricular injection of IL1β
Male and female Iqgap2$^{-/-}$ mice and wildtype littermates were used as experimental animals. All animals were at least 12 weeks old at the time of the surgery. Under isoflurane anesthesia, mice were unilaterally injected into the lateral ventricle using a stereotactic apparatus at coordinates of AP = −0.3 mm, ML = −1 mm, and DV = −3 mm. After injections, mice were returned to prewarmed home cages for recovery. Each mouse received 20 ng/μL of IL1β solution (20 ng in 1 μL PBS) or an equivalent volume of sterile PBS. 24 h after surgery, mice were transcardially perfused with PBS followed by 4% paraformaldehyde and brains were extracted for immunohistological analysis. For quantification, CD45$^+$ cells were manually counted in each section under blinded conditions. Vasculature was labeled using a fluorescence-conjugated GLUT1 antibody to solely quantify CD45$^+$ cells that had extravasated out of the vessels into the brain parenchyma.

Experimental autoimmune encephalomyelitis (EAE)
Female Iqgap2$^{-/-}$ mice and wildtype littermates were used as experimental animals. All animals were between 9 and 13 weeks of age at the time of induction. EAE kits (Hooke Laboratories) targeting MOG$_{35-55}$ antigen were used. 100 μL of MOG$_{35-55}$/Complete Freund's Adjuvant emulsion was injected subcutaneously at the scruff of the neck and near the base of the tail resulting in a total injection volume of 200 μL into each mouse. At 2 and 24 h post injection of emulsion, 100 μL of pertussis toxin (4 μg/mL) was injected intraperitoneally. Clinical scores were evaluated starting 7 days post induction as follows: score 1, flaccid tail; score 2, weak hind limbs; score 3, hindlimb paralysis; score 4, quadriplegia. Clinical scores were recorded every day for the first week after development of symptoms followed by every other day thereafter. Premature deaths were recorded. 30 days following induction, mice were transcardially perfused with PBS followed by 4% paraformaldehyde. Brains and spinal cords were extracted for immunohistological analysis. For quantification, CD45$^+$ cells were manually counted in each section under blinded conditions. Vasculature was labeled using a fluorescence-conjugated GLUT1 antibody to ensure that CD45$^+$ cells had extravasated out of the vessels. For quantifying EAE pathology in spinal cord, total area and demyelination area were calculated using the "Measure" tool in ImageJ by manually outlining regions of interest as indicated by Luxol Fast Blue stain.

Zebrafish maintenance and procedures

For imaging live larvae, 0.003% phenylthiourea (PTU) was used beginning at 1 dpf to inhibit melanin production. These studies used the AB wildtype strains and the transgenic reporter strains (Tg(kdrl:HRAS-mCherry)[s896,78] abbreviated as Tg(kdrl:mCherry), and Tg(mpeg1:EGFP)[gl22,79] abbreviated as Tg(mpeg1:EGFP). Mosaic *iqgap2* crispants were generated by injection of 7 μM Cas9 protein complexed with four sgRNAs (5′-AGTAGCCTCGATTTACAGG-3′, 5′-GCACTTTGTCAGTCACGGAA-3′, 5′-CAGGACAGCGCGAGCA CTG-3′, and 5′-AAAGTCCGCGCG CAGTTTA-3′) to target multiple sites in the *iqgap2* transcript, and *tyr* control crispants were similarly targeted with four sgRNAs (5′-GCCGCACACAGAGCCGTCGC-3′, 5′-GGATGCATTATTACGTGTCC -3′, 5′- GACTCTACATCG GCGGATGT-3′, and 5′-GTATCCGTCGTTGTGTCCGA-3′). To distinguish between microglia and macrophages, 4 dpf larvae were exposed to 2.5 μg/mL of Neutral Red (Millipore Sigma: N7005) in embryo water for 3 h at 28.5°C. Larvae were washed at least three times to remove the residual dye and then microglia were assessed the next day as previously described.[48] Zebrafish larvae were immobilized by tricaine exposure and live imaged on a Leica SP8 line scanning confocal microscope. Quantification of mpeg+ and Neutral Red+ cells was manually performed on blinded z stack images that spanned the entire larval head using ImageJ.

Human brain tissue preparation

Human brain tissue was obtained at autopsy and prepared as previously described.[81] Tissue was immersion fixed in 10% formalin (Thermo Fisher Scientific) at 4°C for 1–3 days. The fixative solution was then removed and the tissued rinsed with 1x TBS (Corning) three times for 5 min each. The tissue was placed in sterile 10% sucrose (Millipore Sigma)/1x TBS/0.02% sodium azide (NaN$_3$, Millipore Sigma) until tissue sank and then 30% sucrose/1x TBS/0.02% NaN$_3$ for overnight at 4°C or until the tissue sank. The tissue block was affixed to the stage of vibratome using cyanoacrylate cement and fully submerged in 1x TBS. Hippocampal and superior temporal lobe sections were prepared at 50 μm thickness. Floating tissue sections were transferred to 15 mL Falcon tubes with antigen retrieval buffer (10 mM citric acid pH 6.0, Millipore Sigma) containing 0.05% Tween 20 (Millipore Sigma) and heated to 95°C for 20 min in a block heater. Sections were then washed with 100 mM glycine (Millipore Sigma)/1x TBS/0.1% Triton X-100 (Millipore Sigma) buffer for 30 min followed by permeabilization with 0.3% Triton X-100/1x TBS buffer for 30 min and two washes for 5 min each with 1x TBS at room temperature.

Development of a custom antibody against human IQGAP2 protein

A peptide corresponding to amino acid residues 1460–1474 of human IQGAP2 (RSIKLDGKGEPKGAK) was synthesized with an amino-terminal cysteine and conjugated to maleimide-activated Keyhole Limpet Haemocyanin (KLH), maleimide-activated bovine serum albumin (BSA), and SulfoLink resin using manufacturer protocols (Thermo Fisher). The peptide-KLH conjugate was used to immunize rabbits (Cocalico Biologicals). Rabbit antisera were tested for the presence of antibodies recognizing the IQGAP2 peptide by dot blot analysis using the peptide-BSA conjugate. The rabbit antibodies were affinity-purified from the antisera using the peptide-SulfoLink resin, where 5 mL of rabbit sera was diluted 1:1 with PBS and passed over a 2 mL peptide-SulfoLink column. After extensive washing with PBS, bound antibodies were eluted with 8.5 mL 0.1 M Glycine (pH 2.2) and collected in a tube containing 1.5 mL of 1 M Tris (pH 8). Antibody solution was stored at −80°C. Antibody specificity was assessed in Caco-2 cells as described below (Figure S11).

Caco-2 cell procedures for evaluating human IQGAP2 antibody specificity

For IQGAP2 knockdown, siRNA Dicer-substrate interfering RNAs (Integrated DNA Technologies) were used through the protocol of Oligofectamine Transfection Reagent (Thermo Fisher). The cells were incubated for 72 h before protein extraction.

For IQGAP2 knockout, Caco-2 cells were washed once with DPBS, incubated with TrypLE Express for 3 min at 37°C, and collected via centrifugation. The resultant single-cell suspension was analyzed using a Countess II (Thermo Fisher) automated hemacytometer to determine live cell count. Measured density was used to determine appropriate transduction parameters. Cells were transduced at a multiplicity of infection (MOI) of 0.3 with Edit-R lentiviral mKate2-tagged, constitutively expressed Cas9 nuclease (Dharmacon) under the hEF1α promoter in transduction medium containing 5 μg/mL polybrene (EMD Millipore). Complete growth medium was added to transduced cells at a 3:1 dilution 5 h after initiation of transduction. Complete media was changed at 48 h post transduction initiation. Fresh medium was replaced every 48 h until cells were confluent for passaging. These polyclonal Cas9-expressing Caco-2 cells were then transfected with crRNA:tracrRNA mixes delivered in DharmaFECT transfection reagent. Briefly, custom crRNA and tracrRNA were reconstituted and transfection mixes were prepared and incubated at room temperature for 20 min. Cells were transfected overnight and then cultured for 72 h before protein extraction.

Immunofluorescent staining
Mouse tissue

Tissue slices were retrieved from the −80°C freezer and allowed to thaw at room temperature for 10–15 min. Sections were washed with 1X PBS with 0.03% Triton X-100 to remove the OCT medium. Sections were then blocked using a goat serum blocking buffer and incubated in primary antibody solution overnight at 4°C. After incubation, primary antibody solution was thoroughly washed off and sections were incubated in secondary antibody solution for 2 h at room temperature. All antibodies and corresponding dilutions used for immunohistochemistry are listed in Tables S3 and S4. Following final washes, tissue was mounted in Prolong Gold Antifade Mountant with DAPI (Invitrogen) and slides were allowed to dry overnight before imaging on a Leica DMi8 epifluorescence

microscope. For microglial morphological analysis, 20 μm thick z stack images were acquired with a step-size of 0.5 μm. All acquired images were processed and quantified using ImageJ software. For quantification of vascular Vcam1 expression, mean Vcam1 intensity was calculated within CD31$^+$ vessels using ImageJ. Image processing pipeline for microglia quantification and morphological analysis using Iba-1 was adapted from previously established protocols.[84,85]

Human tissue

Immunohistochemical labeling in hippocampal tissue slices was performed as previously described[86,87] with minor modifications. All antibodies and corresponding dilutions used for immunohistochemistry are listed in Tables S3 and S4. For detection of IQGAP2 expression in AD and non-AD tissue, slices were incubated with primary antibodies for 48 h at 4°C followed by secondary antibodies for 2 h at room temperature. Neuritic plaques, neurofibrillary tangles and related AD pathological structures were additionally stained using 1 μM 4,4'-[(2-methoxy-1,4-phenylene) di-(1*E*)-2,1-ethenediyl] bisphenol (MX-04) (Tocris) for 15 min at room temperature. Confocal images were acquired using the Zeiss LSM 710 confocal laser-scanning microscope (Carl Zeiss AG) with a 20× air/dry or 63× oil objective and 10 μm z stack scanning projections with a step interval of 1 μm or one scanning projection, with a minimum resolution of 1500 x 1500 pixels. Vascular IQGAP2 expression was quantified using mean IQGAP2 intensity within collagen+ area and parenchymal IQGAP2 expression was quantified by gating collagen-area using ImageJ. For co-labelling IQGAP2 with CNS cell-type specific markers, sections were blocked using 5% of Bovine Serum Albumin (RPI) and 10% normal donkey serum (Invitrogen) for 60 min and placed under the LED lamp BESTVA DC Series 1200W LED full spectrum light array at 4°C overnight for photobleaching. The disappearance of autofluorescence was checked by fluorescence microscopy before continuing with primary antibody and appropriate secondary antibody incubation. The confocal images were acquired using the Zeiss LSM 710 confocal laser-scanning microscope (Carl Zeiss AG) with a 20× air/dry and 10 μm z stack scanning projections with a step interval of 1 μm, with a minimum resolution of 2000 x 2000 pixels. All representative images are maximum projections of acquired z-stacks.

Luxol Fast Blue staining

Tissue slices were retrieved from the −80°C freezer and allowed to thaw at room temperature for 10–15 min. Sections were first allowed to dry overnight at room temperature and then immersed in a 70% ethanol solution overnight to facilitate defatting. Luxol Fast Blue stain (Abcam) was applied to the sections and incubated for 5 to 6 h at 60°C. Excess stain was washed off by consecutive dipping in fresh absolute ethanol. Slides were differentiated briefly using lithium carbonate solution and washed with distilled water and alcohol solution. Lastly, sections were counterstained with Cresyl Etch Violet, washed with distilled water, dehydrated with absolute alcohol and mounted in DPX mounting medium (Sigma-Aldrich). Mounting medium was cured overnight before imaging on a Leica DMi8 inverted microscope.

Western blotting (mouse tissue)

Protein samples were prepared by diluting 20–40 μg of protein with 1X Laemmli buffer (Biorad) supplemented with beta-mercaptoethanol (Sigma) and Ultrapure water (Gibco) to a final volume of 20–30 μL. Samples were then boiled at 95°C for 5 min, cooled on ice, and centrifuged briefly. Samples were then loaded into 4–20% Criterion TGX Midi protein gels (Biorad) along with Precision Plus Dual Color Protein ladder (Biorad) and run at 80-120V. Protein gels were then transferred onto iBlot2 Nitrocellulose membranes (Thermo Fisher Scientific) using an iBlot2 transfer device (Thermo Fisher Scientific). Membranes were cut to size and blocked for at least 30 min at room temperature in Intercept TBS Blocking buffer (LI-COR Biosciences) on a shaker. Membranes were submerged in primary antibodies diluted in blocking buffer with 0.05% Tween 20 (Sigma) and incubated at 4°C overnight. Following primary antibody incubation, membranes were washed in wash buffer (1X tris-buffered saline with 0.05% Tween 20). Membranes were incubated in secondary antibodies diluted in the wash buffer at room temperature for 2 h. All primary and secondary antibody information is listed in Tables S3 and S4. Blots were imaged using an LI-COR Odyssey Clx or Fc Imager and bands were quantified using Image Studio Lite software.

Western blotting (human cells)

40 μg of total protein was resolved in precast 4–20% gradient Mini-PROTEAN TGX gels (Bio-Rad) and run at 120V. Proteins were transferred onto Trans-Blot Turbo Mini 0.2 μm PVDF membranes (Bio-Rad) using Trans-Blot Turbo (Bio-Rad). Subsequently, membranes were blocked for 1 h with 5% non-fat milk. Primary antibody was incubated at 4°C overnight, followed by extensive washes and incubation with secondary antibody for 1 h at room temperature. All primary and secondary antibody information is listed in Tables S3 and S4. Membranes were washed again and developed using SuperSignal Chemiluminescent Substrate and Chemidoc Imaging System (Bio-Rad).

Single-cell RNA sequencing

Fresh cortical tissue was homogenized and delipidated using an Adult Brain Dissociation Kit (Miltenyi Biotec) according to the manufacturer's instructions. The resultant single-cell suspension was incubated with TruStain FcX (Biolegend) for 10 min at 4°C to prevent non-specific antibody binding of Fc receptors, labeled with a secondary conjugated CD31 antibody (1:2000, eBioscience) for 30 min, and counterstained with DAPI. Live CD31$^+$ cells were flow sorted using a 4-laser FACS Aria III sorter (BD Biosciences) at the Vanderbilt Flow Cytometry Shared Resource. Live cells were resuspended in DMEM (Gibco) supplemented with 2% FBS to

obtain a concentration of 700–1200 cells/μL. RNA extraction, 10X Genomics Chromium 5′ scRNAseq Library Prep, and sequencing on an Illumina NovaSeq6000 sequencer was performed at the VANTAGE core facility.

Single-cell RNA sequencing analysis

All gene by counts data were read into Seurat (v.4). The initial data were filtered to retain only cells with RNA counts between 1,200 and 20,000 (with less than 10% being mitochondrial). Within each biological experiment, data were log normalized. The top 2,000 variable features (as identified by variance) were selected. Samples were combined using CCA (Seurat v.4) and then standardized. UMAP based on the first 50 principal components was used to reduce dimensionality for visualization and clustering.[88] Predicted doublets were filtered out using DoubletFinder.[89] Unsupervised clustering was achieved using the KNN-graph approach in Seurat,[80] and clusters were annotated with SingleR[90] based on previously published datasets.[49] Predominantly endothelial clusters (0,2,4,5) were rescaled and clustered based on the first 15 principal components. Clusters were annotated as arterial, capillary, or venous based on the expression of established marker gene sets.[21] Approximately 2,000 ECs were analyzed per condition. Differentially expressed genes (DEGs) were computed in Seurat using the FindMarkers() function with built-in Bonferroni correction. KEGG or Reactome gene set enrichment analysis (GSEA) was computed on significant DEGs using WebGestalt with a false discovery rate cutoff of 0.05 and weighted set cover redundancy reduction.[91] Communication between cell types was predicted using the CellChat R packages.[59] For visualization, *EnhancedVolcano*,[92] *UpSetR* shiny app,[93] *iGraph*,[94] and *ggvenn* were employed.

QUANTIFICATION AND STATISTICAL ANALYSIS

Statistical analysis for single-cell RNA sequencing data was conducted in R. All other analysis was performed in GraphPad Prism 9.0.0 and 10.4.0. Statistical details of experiments such as statistical test used, exact value of n, what n represents, definition of center and measure of variability are included in corresponding figure legends. Data are represented as mean ± SD and a p-value of less than 0.05 was considered statistically significant. For comparisons between two groups, statistical significance was calculated using Student's t test. For comparisons between multiple groups, statistical significance was calculated using analysis of variance and Tukey's multiple comparisons test where applicable. Log rank (Mantel-Cox) test was used to calculate statistical significance for probability of survival. Wilcoxon-rank order test with Bonferroni correction was used to analyze differential gene expression. p values are represented as *($p < 0.05$), **($p < 0.01$), ***($p < 0.001$), and ****($p < 0.0001$).